GaN-based diodes and transistors for chemical, gas, biological and pressure sensing

2004 J. Phys.: Condens. Matter 16 R961

(http://iopscience.iop.org/0953-8984/16/29/R02)

INSTITUTE OF PHYSICS PUBLISHING JOURNAL OF PHYSICS: CONDENSED MATTER

J. Phys.: Condens. Matter **16** (2004) R961–R994 PII: S0953-8984(04)78067-4

TOPICAL REVIEW

GaN-based diodes and transistors for chemical, gas, biological and pressure sensing

S J Pearton[1], B S Kang[2], Suku Kim[2], F Ren[2], B P Gila[1], C R Abernathy[1], Jenshan Lin[3] and S N G Chu[4]

[1] Department of Materials Science and Engineering, University of Florida, Gainesville, FL 32611, USA
[2] Department of Chemical Engineering, University of Florida, Gainesville, FL 32611, USA
[3] Department of Electrical Engineering, University of Florida, Gainesville, FL 32611, USA
[4] Multiplex Inc., South Plainfield, NJ 07080, USA

Received 18 March 2004
Published 9 July 2004
Online at stacks.iop.org/JPhysCM/16/R961
doi:10.1088/0953-8984/16/29/R02

Abstract

There is renewed emphasis on development of robust solid-state sensors capable of uncooled operation in harsh environments. The sensors should be capable of detecting chemical, gas, biological or radiation releases as well as sending signals to central monitoring locations. We discuss the advances in use of GaN-based solid-state sensors for these applications. AlGaN/GaN high electron mobility transistors (HEMTs) show a strong dependence of source/drain current on the piezoelectric polarization-induced two-dimensional electron gas (2DEG). Furthermore, spontaneous and piezoelectric polarization-induced surface and interface charges can be used to develop very sensitive but robust sensors to detect gases, polar liquids and mechanical pressure. AlGaN/GaN HEMT structures have been demonstrated to exhibit large changes in source–drain current upon exposing the gate region to various block co-polymer solutions. Pt-gated GaN Schottky diodes and Sc_2O_3/AlGaN/GaN metal-oxide semiconductor diodes also show large change in forward currents upon exposure to H_2. Of particular interest is detection of ethylene (C_2H_4), which has strong double bonds and hence is difficult to dissociate at modest temperatures. Apart from combustion gas sensing, the AlGaN/GaN heterostructure devices can be used as sensitive detectors of pressure changes. In addition, large changes in source–drain current of the AlGaN/GaN HEMT sensors can be detected upon adsorption of biological species on the semiconductor surface. Finally, the nitrides provide an ideal platform for fabrication of surface acoustic wave (SAW) devices. The GaN-based devices thus appear promising for a wide range of chemical, biological, combustion gas, polar liquid, strain and high temperature pressure-sensing applications. In addition, the sensors are compatible with high bit-rate wireless communication systems that facilitate their use in remote arrays.

(Some figures in this article are in colour only in the electronic version)

Contents

1. Introduction 962
2. Sensors based on AlGaN/GaN heterostructures 965
   - 2.1. Gateless AlGaN/GaN HEMT response to block co-polymers 965
   - 2.2. Hydrogen gas sensors based on AlGaN/GaN-based metal-oxide semiconductor diodes 968
   - 2.3. Hydrogen-induced reversible changes in Sc_2O_3/AlGaN/GaN HEMTs 970
   - 2.4. Effect of external strain on conductivity of AlGaN/GaN HEMT 974
   - 2.5. Pressure sensor fabrication 978
   - 2.6. Selective-area substrate removal 980
   - 2.7. Biosensors using AlGaN/GaN heterostructures 983
   - 2.8. Surface-acoustic-wave- (SAW-) based biosensors 985
   - 2.9. Surface acoustic wave device fabrication 987
   - 2.10. Surface acoustic wave device for gas sensing 989
   - 2.11. Flexural plate wave (FPW) device for liquid sensing 989
   - 2.12. SAW array 989
   - 2.13. Wireless sensor network and wireless sensor array using RFID technology 990
3. Summary 991

Acknowledgments 992

References 992

1. Introduction

AlGaN/GaN high electron mobility transistors (HEMTs) have demonstrated extremely promising results for use in broad band power amplifiers in base station applications due to the high sheet carrier concentration, electron mobility in the two-dimensional electron gas (2DEG) channel and high saturation velocity [1–10]. The high electron sheet carrier concentration of nitride HEMTs is induced by piezoelectric polarization of the strained AlGaN layer and spontaneous polarization is very large in wurtzite III nitrides [6–9]. This suggests that nitride HEMTs are excellent candidates for pressure sensor and piezoelectric-related applications. Payoffs relative to Si field effect transistors (FETs) include being chemically inert in electrolyte solutions (low linear drift), sensitivity of $\sim$57 mV/pH, cf other potential gate materials such as SiO_2 (32–40 mV/pH), Al_2O_3(57) and Ta_2O_5(58.5), and the ability to integrate with blue or ultra-violet light-emitting diodes (LEDs) for directed cell growth or remediation and also integration with chemical/pressure sensors and off-chip communications circuitry (either by photonic or electrical means).

Unlike conventional III–V-based HEMTs, such as those in the AlGaAs/GaAs system, there is no dopant in the typical nitride-based HEMT structure and all the layers are undoped. The carriers in the two-dimensional electron gas (2DEG) channel are induced by piezoelectric polarization of the strained AlGaN layer and spontaneous polarization, both of these effects being very large in wurtzite III nitrides. Carrier concentrations $>10^{13}$ cm^{-3} can be obtained in the 2DEG, which is five times larger than that in the more conventional AlGaAs/GaAs material system. The portion of the carrier concentration induced by the piezoelectric effect is around 45–50%. This makes nitride HEMTs excellent candidates for pressure sensor and piezoelectric-related applications.

There is a strong interest in wide bandgap semiconductor gas sensors for applications including fuel leak detection in spacecraft and release of toxic or corrosive gases. In addition, these detectors would have dual use in automobiles and aircraft, fire detectors, exhaust diagnosis

and emissions from industrial processes. Wide bandgap semiconductors such as GaN and SiC are capable of operating at much higher temperatures than more conventional semiconductors such as Si because of their large bandgap (3.4 eV for GaN, 3.26 eV for the 4H-SiC poly-type versus 1.1 eV for Si). The ability of these materials to function in high temperature, high power and high flux/energy radiation conditions will enable large performance enhancements in a wide variety of spacecraft, satellite and radar applications. GaN and SiC uncooled electronics and sensors will reduce spacecraft launch weights and increase satellite functional capabilities. Given the high cost per pound of launching payloads into earth orbit, the weight savings gained by using wide bandgap devices could have large economic and competitive implications in the satellite industry. Existing commercial satellites require thermal radiators to dissipate heat generated by the spacecraft electronics. These radiators could be eliminated with GaN and SiC, and allow greater functionality (more transponders in a commercial satellite) by utilizing the space and weight formerly occupied by the thermal management system. In addition, the radiation hardness of these materials would reduce the weight of shielding normally used to protect spacecraft electronic components from radiation. Simple Schottky diode or field-effect transistor structures fabricated in GaN and SiC are sensitive to a number of gases, including hydrogen and hydrocarbons. An additional attractive attribute of GaN and SiC is the fact that gas sensors based on this material could be integrated with high temperature electronic devices on the same chip. While there has been extensive development of SiC-based gas sensors [11–25], the work on GaN is at an earlier stage [26, 27], but there has been much recent activity based on the relative advantages of GaN for sensing [26–40]. These advantages include the presence of the polarization-induced charge, the availability of a heterostructure and the more rapid pace of device technology development for GaN which borrows from the commercialized light-emitting diode and laser diode businesses.

Wide bandgap electronics and sensors based on GaN can be operated at elevated temperatures (600 °C, or 1112 F, glowing red hot) where conventional Si-based devices cannot function, being limited to <350 °C. This is due to its low intrinsic carrier concentration at high temperature, as shown in figure 1. The ability of these materials to function in high temperature, high power and high flux/energy radiation conditions will enable large performance enhancements in a wide variety of spacecraft, satellite, homeland defence, mining, automobile, nuclear power and radar applications. In addition there appear to be applications for high temperature pressure sensing for coal and fossil energy applications. AlGaN/GaN heterojunction HEMTs grown on SiC substrates have demonstrated extremely promising results for use as power amplifiers in many analogue applications due to the high sheet carrier concentration, electron mobility in the two-dimensional electron gas (2DEG) channel and high saturation velocity, as illustrated in figure 2 [41].The demonstrated power densities from these devices are well in excess of those possible with GaAs, Si or SiC. The ability to integrate these with GaN-based LEDs is a powerful driver for highly integrated sensor systems. Figure 3 shows examples of concepts that employ GaN LEDs for directed cell growth or for causing fluorescence for identification of DNA fragments in a microfluidic array. In the latter case, the fluid containing the DNA is placed in a microfluidic channel and the uncharged DNA fragments in the laminar flow region in the centre of the channel are not affected by voltages applied to the gold tabs on the surface of the channel. However, the applied field acts to pull charged fragments to the non-laminar region at the edge of the channel, where they can be separated from the main flow. The integrated, embedded LEDs can be used to induce fluorescence from these separated fragments.

The charges in the two-dimensional (2D) channel of AlGaN/GaN HEMTs are induced by spontaneous and piezoelectric polarization, which are balanced with positive charges on the surface. Figure 4 shows schematic diagrams of the direction of the spontaneous and

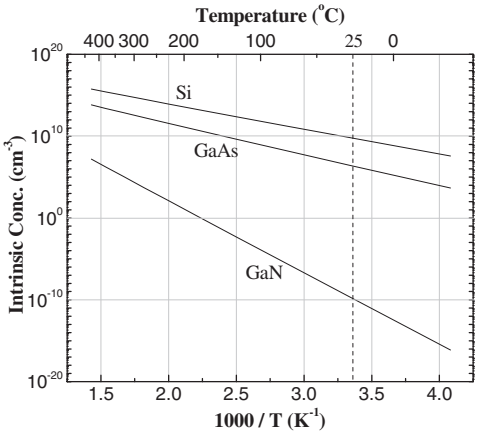

Figure 1. Intrinsic carrier concentration as a function of temperature.

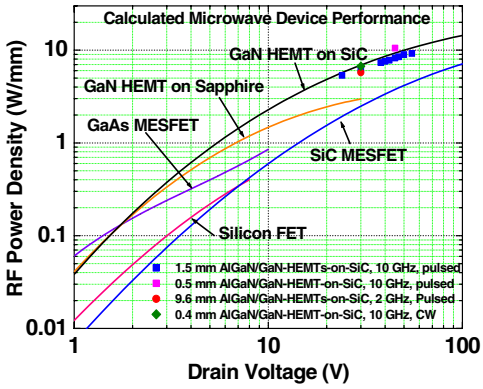

Figure 2. Performance of GaN/AlGaN-based power amplifier as compared to GaAs-, Si- and SiC-based devices.

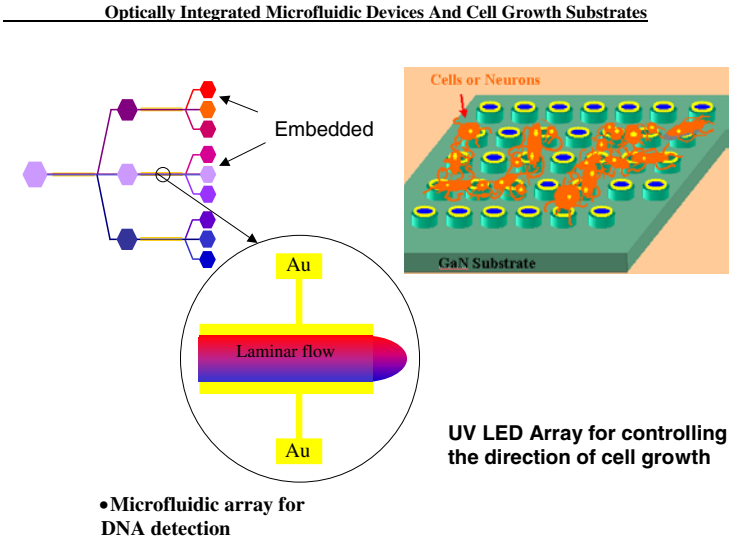

Figure 3. Schematic diagram of optically integrated microfluidic devices and cell-growth substrates based on GaN.

piezo-electric polarization in both Ga and N face wurtzite GaN crystals [42]. The induced sheet carrier concentration of undoped Ga-face AlGaN/GaN can be calculated by following equation [43]:

$$n_s(x) = \frac{\sigma(x)}{e} - \left(\frac{\varepsilon_0\varepsilon(x)}{d_d e^2}\right)(e\phi_b(x) + E_F(x) - \Delta E_C(x)) \tag{1}$$

where ε_0 is the electric permittivity, $\varepsilon(x) = 9.5 - 0.5x$ is the relative permittivity, x is the Al mole fraction of $Al_xGa_{1-x}N$, d_d is the AlGaN layer thickness, $e\phi_b$ is the Schottky barrier of the gate contact on AlGaN ($e\phi_b(x) = 0.84 + 1.3x$ (eV)), E_F is the Fermi level ($E_F(x) = [9he^2n_s(x)/16\varepsilon_0\varepsilon(x)\sqrt{(8m * (x))}]^{2/3} + h^2n_s(x)/4\pi m * (x)$), E_c is the conduction band ($E_g(x) = 6.13x + 3.42(1-x) - x(1-x)$ (eV)) and ΔE_c is the conduction

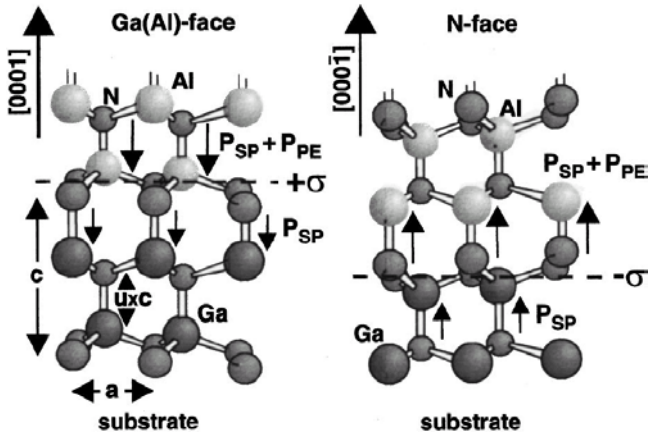

Figure 4. Piezoelectric (PE) and spontaneous polarization (SP) effects in Ga(Al) or N-face AlGaN/GaN heterostructures (after [57] and [42]).

band discontinuity between AlGaN and GaN ($\Delta E_c(x) = 0.7[E_g(x) - E_g(0)]$). Note that $m*(x) \sim 0.228$. Therefore, the sheet charge density in the 2D channel of AlGaN/GaN HEMT is extremely sensitive to its ambient. The adsorption of polar molecules on the surface of GaN affects both the surface potential and resulting device characteristics.

Without any surface passivation the sheet carrier concentration of the polarization-induced 2DEGs confined at interfaces of AlGaN/GaN HEMTs becomes sensitive to any manipulation of surface charge. This effect is used to build micro-sensors which are able to detect applied strain and surface polarity change by polar liquids or toxic gases. Beside the basic physics of polarization-induced charges at surfaces and interfaces and the formation of 2DEGs in piezoelectric AlGaN/GaN heterostructures we will summarize the present status and future concepts of novel AlGaN/GaN-based chemical and biological sensor systems.

In this review, the components for building high temperature chemical, gas and pressure sensors are discussed in addition to the emerging work on using AlGaN/GaN heterostructures as biosensors. Numerous groups have demonstrated the feasibility of AlGaN/GaN heterostructure-based hydrogen detectors with extremely fast time response and capable of operating at high temperature (500–800 °C), eliminating bulky and expensive cooling systems [26–37]. In addition, gateless AlGaN/GaN HEMTs show a strong dependence of source/drain current on the polarity and concentration of polymer solutions [39]. There have also been recent reports of the investigation of the effect of external strain on the conductivity of an AlGaN/GaN high electron mobility transistor [40]. It is also possible to employ selective substrate removal techniques such as laser drilling to etch off the SiC substrate and realize an AlGaN/GaN membrane for pressure sensor. These can be used for inexpensive low weight pressure monitoring applications.

2. Sensors based on AlGaN/GaN heterostructures

2.1. Gateless AlGaN/GaN HEMT response to block co-polymers

Gateless AlGaN/GaN high electron mobility transistor (HEMT) structures exhibit large changes in source–drain current upon exposing the gate region to various block co-polymer solutions [39]. The polar nature of some of these polymer chains lead to a change of

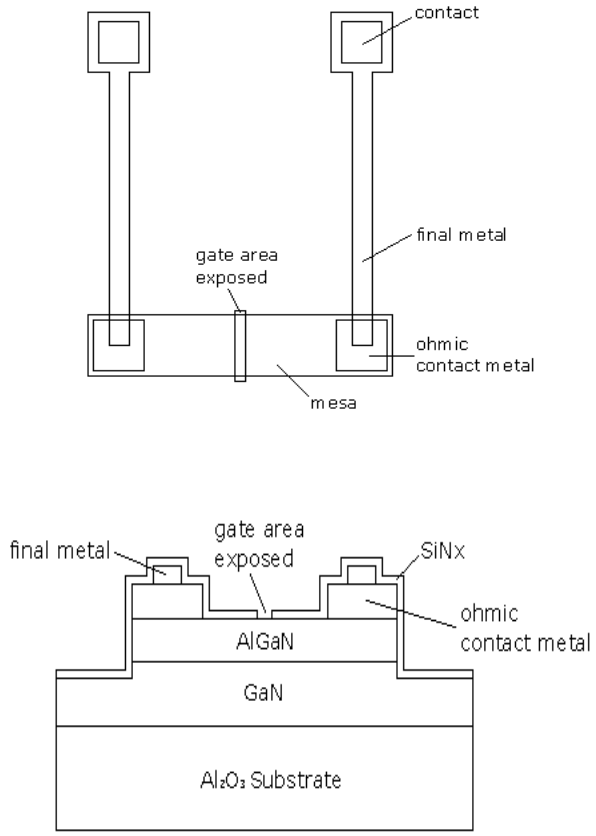

Figure 5. Schematic layout of gateless HEMT structures (top) and device cross-section (bottom).

surface charges in gate region on the HEMT, producing a change in surface potential at the semiconductor/liquid interface. The structure was grown by metal organic chemical vapour deposition at 1040 °C on *c*-plane Al_2O_3 substrates and then fabricated into a gateless HEMT. Silicon nitride was used to encapsulate the source/drain regions, with only the gate region open to allow the polar liquids to reach across the surface.

A schematic diagram of the device is shown in figure 5 with both the plan view layout and cross-sectional view. The source–drain current–voltage characteristics were measured at 25 °C using an Agilent 4156C parameter analyser with the gate region exposed either to air or various concentrations of the block co-polymers and individual polymers. The block copolymers are composed of different proportions of the individual polymers, PS and PEO.

Due to the parasitic resistance induced by the large gate dimension ($20 \times 150\ \mu m^2$) i, the drain current did not reach saturation at 40 V. If the device dimension were reduced, larger changes of drain current should be expected. The dipole moment of ethylene and styrene monomer are 1.89 and 0.62, respectively [33]. The dipole moment of the ethylene monomer is three times larger than that of styrene monomer; however, the effect of PEO solutions on the drain current of the nitride HEMT is only half of the PS styrene. This could be due to PEO being extremely linear with its dipole oriented along the polymer chain. The $20 \times 150\ \mu m^2$ gate opening is much larger than the individual monomer in the PEO chain. Therefore, the dipole effect on the device is very local within the big gate opening and some of the net surface charge induced by the PEO is cancelled out. In the case of PS, the polymer chain is very bulky and not very linear; the net dipole induced charge may be higher than that of PEO; therefore,

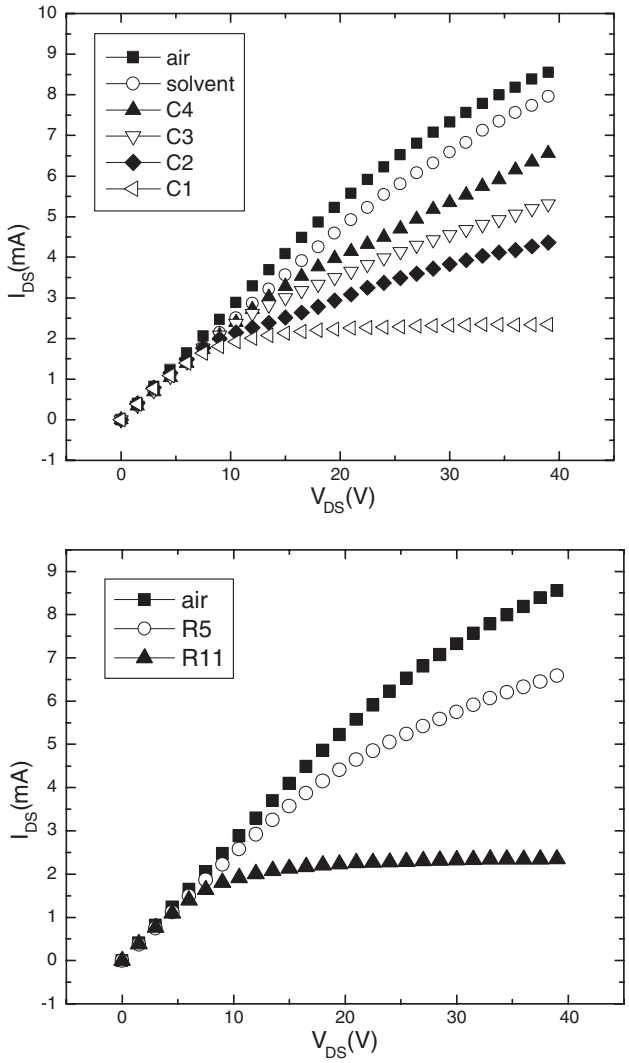

Figure 6. Drain I–V characteristics for the different concentrations of the copolymer solutions, $C_1 = 1.0917$ mg ml^{-1}, $C_2 = 0.7612$ mg ml^{-1}, $C_3 = 0.5504$ mg ml^{-1}, $C_4 = 0.087\,34$ mg ml^{-1} (top). The drain I–V characteristics of copolymers with different compositions (R_5, MW = 66.6 kg mol^{-1}, 53% of PS and 47% of PEO, and R_{11}, MW 58.8 kg mol^{-1}, 71% of PS and 29% of PEO) (bottom).

larger drain current changes were observed. If the gate dimension reduces to the size of an individual monomer, the opposite trends may be obtained.

The concentration of the block copolymer also affected the changes of the drain current, as shown in figure 6 (top). The molecular weight of the copolymer is 58.8 kg mol^{-1} and it contains 71% of PS and 29% PEO. The concentration of the copolymer was varied from 1.0917 to 0.087 34 mg ml^{-1}. As the copolymer concentration increased, the drain current reduced more. Copolymer with similar molecular weight, but different compositions, also had significant impact on the drain IV characteristics. As shown in figure 6 (bottom), the copolymer with a large percentage of PS reduced the drain current more.

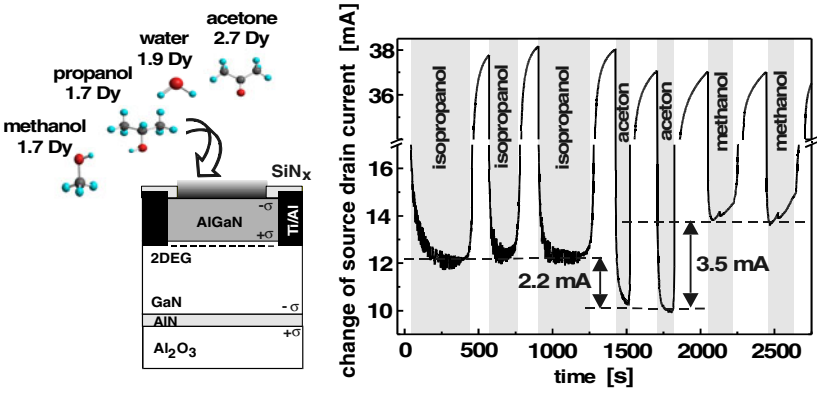

Figure 7. Time dependence of changes in source–drain current in gateless HEMTs exposed to ionic liquids with different dipole moments (after [29]).

Eickhoff *et al* [33] have reported on the time dependence of changes in source–drain current of gateless HEMTs exposed to polar liquids with different dipole moments. As shown in figure 7, the HEMTs show very large changes in current as the different polar liquids are introduced to the surface. However the magnitude of the changes did not correlate with the dipole moment of the liquids, suggesting that steric hindrance effects or the exact orientation of the molecule when it adsorbs on the surface must play a role.

In summary, gateless AlGaN/GaN HEMTs show a strong dependence of source/drain current on the polarity and concentration of polymer or polar liquid solutions. These can be used as sensitive pH meters. These data suggest the possibility of functionalizing the surface for application as biosensors, especially given the excellent stability of the GaN and AlGaN surfaces which should minimize degradation of adsorbed cells.

2.2. Hydrogen gas sensors based on AlGaN/GaN-based metal-oxide semiconductor diodes

Simple GaN Schottky diodes exhibit strong changes in current upon exposure to hydrogen-containing ambients [27–35]. The effect is thought to be due to a lowering of the effective barrier height as molecular hydrogen catalytically cracks on the metal gate (typically made of Pt) and atomic hydrogen diffuses to the interface between the metal and GaN, altering the interfacial charge. Steinhoff *et al* [29] found that it was necessary to have a native oxide present between the semiconductor and the gate metal in order to see significant current changes. Thus it is desirable to specifically incorporate an oxide into GaN-based diodes or HEMTs in order to maximize the hydrogen detection response.

Gas sensors based on an MOS diode on an AlGaN/GaN high electron mobility transistor (HEMT) layer structure are of interest, because HEMTs are expected to be the first GaN electronic device that is commercialized, as part of next generation radar and wireless communication systems. These structures have much higher sensitivity than Schottky diodes on a GaN layer, because they are true transistors and therefore operate with gain. In addition, the MOS-gate version of the HEMT has significantly better thermal stability than a metal-gate structure [38, 44–51] and is well suited to gas sensing. When exposed to changes in ambient, changes in the surface potential will lead to large changes in channel current.

A typical HEMT gas sensor employs Ohmic contacts formed by lift-off of e-beam-deposited Ti (200 Å)/Al (1000 Å)/Pt (400 Å)/Au (800 Å). The contacts are annealed at 850 °C for 45 s to minimize the contact resistance. Thin (typically 400 Å thick) gate dielectrics of

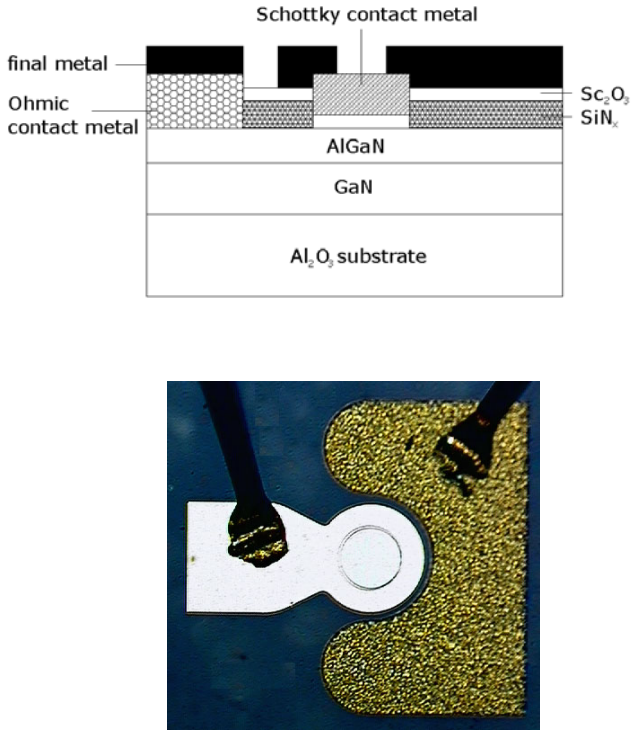

Figure 8. Cross-sectional schematic diagram of completed MOS diode on AlGaN/GaN HEMT layer structure (top) and plan-view photograph of device (bottom).

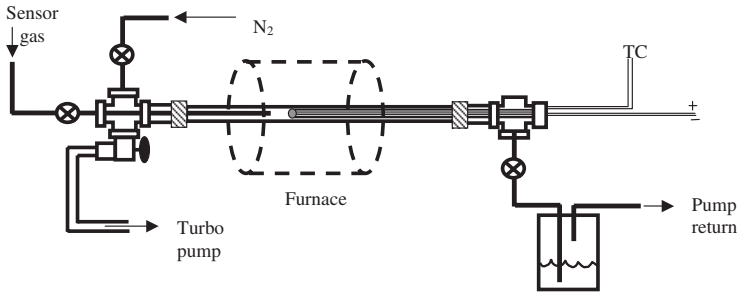

Figure 9. Schematic diagram of environmental test chamber into which different gases can be introduced and the GaN-based sensors tested at different temperatures under different gas ambients.

MgO or Sc_2O_3 are deposited through a contact window of SiN_x. The dielectrics are deposited by rf plasma-activated MBE at 100 °C using elemental Mg or Sc evaporated from a standard effusion all at 1130 °C and O_2 derived from an Oxford RF plasma source [49]. 200 Å Pt Schottky contacts are deposited on the top of Sc_2O_3. Then, final metal e-beam-deposited Ti/Au (300 Å/1200 Å) interconnection contacts were employed on the MOS-HEMT diodes. Figure 8 shows a schematic diagram (left) and photograph (right) of the completed device. The devices are bonded to electrical feed-throughs and exposed to different gas ambients in an environmental chamber. A schematic diagram of the chamber is shown in figure 9.

As the detection temperature is increased, the response of the MOS-HEMT diodes increases due to more efficient cracking of the hydrogen on the metal contact. Pt is a good choice as the contact due to its efficiency at cracking hydrogen at relatively low temperatures, but for applications requiring more thermally stable contacts we have also found that W is effective at higher operating temperatures (300 °C).

The threshold voltage for a MOSFET is given by [43]

$$V_T = V_{FB} + 2\phi_B + \left(\frac{4eN_D\phi_B\varepsilon_S}{C_i}\right)^{0.5} \tag{2}$$

where V_{FB} is the voltage required for flat band conditions, ϕ_B the barrier height, e the electronic charge and C_i the Sc_2O_3 capacitance per unit area. In analogy with results for MOS gas sensors in other materials systems [20], the effect of the introduction of the atomic hydrogen into the oxide is to create a dipole layer at the oxide/semiconductor interface that will screen some of the piezo-induced charge in the HEMT channel.

To test the time response of the MOS diode sensors, the 10% H_2/90% N_2 ambient was switched into the chamber through a mass flow controller for periods of 10, 20 or 30 s and then switched back to pure N_2. Figure 10 (left) shows the time dependence of forward current at a fixed bias of 2 V under these conditions. The response of the sensor is rapid (<1 s), with saturation taking almost the full 30 s. Upon switching out of the hydrogen-containing ambient, the forward current decays exponentially back to its initial value. This time constant is determined by the volume of the test chamber and the flow rate of the input gases and is not limited by the response of the MOS diode itself. Figure 10 (right) shows the time response of the forward current at fixed bias to a series of gas injections into the chamber, of duration 10 s each (top) or 30 s each (bottom). The MOS diode shows good repeatability in its changes of current and the ability to cycle this current in response to repeated introductions of hydrogen into the ambient. Once again, the response appears to be limited by the mass transport of gas into and out of the chamber and not to the diffusion of hydrogen through the Pt/Sc_2O_3 stack.

AlGaN/GaN MOS-HEMT diodes appear well suited to combustion gas sensing applications. The changes in forward current are approximately double those of simple GaN Schottky diode gas sensors tested under similar conditions and suggest that integrated chips involving gas sensors and HEMT-based circuitry for off-chip communication are feasible in the AlGaN/GaN system.

2.3. Hydrogen-induced reversible changes in Sc_2O_3/AlGaN/GaN HEMTs

Pt-contacted AlGaN/GaN high electron mobility transistors with Sc_2O_3 gate dielectrics show reversible changes in drain–source current upon exposure to H_2-containing ambients, even at room temperature. The changes in current (as high as 3 mA for relatively low gate voltage and drain–source voltage) are approximately an order of magnitude larger than for Pt /GaN Schottky diodes and a factor of five larger than Sc_2O_3/AlGaN/GaN metal-oxide semiconductor (MOS) diodes exposed under the same conditions. This shows the advantage of using a transistor structure in which the gain produces larger current changes upon exposure to hydrogen-containing ambients. The increase in current is the result of a decrease in effective barrier height of the MOS gate of 30–50 mV at 25 °C for 10% H_2/90% N_2 ambients relative to pure N_2 and is due to catalytic dissociation of the H_2 on the Pt contact, followed by diffusion to the Sc_2O_3/AlGaN interface.

Figure 11 (top) shows the MOS-HEMT drain–source current–voltage (I_{DS}–V_{DS}) characteristics at 25 °C measured in both the pure N_2 and 10% H_2/90% N_2 ambients. The current is measurably larger in the latter case as would be expected if the hydrogen catalytically

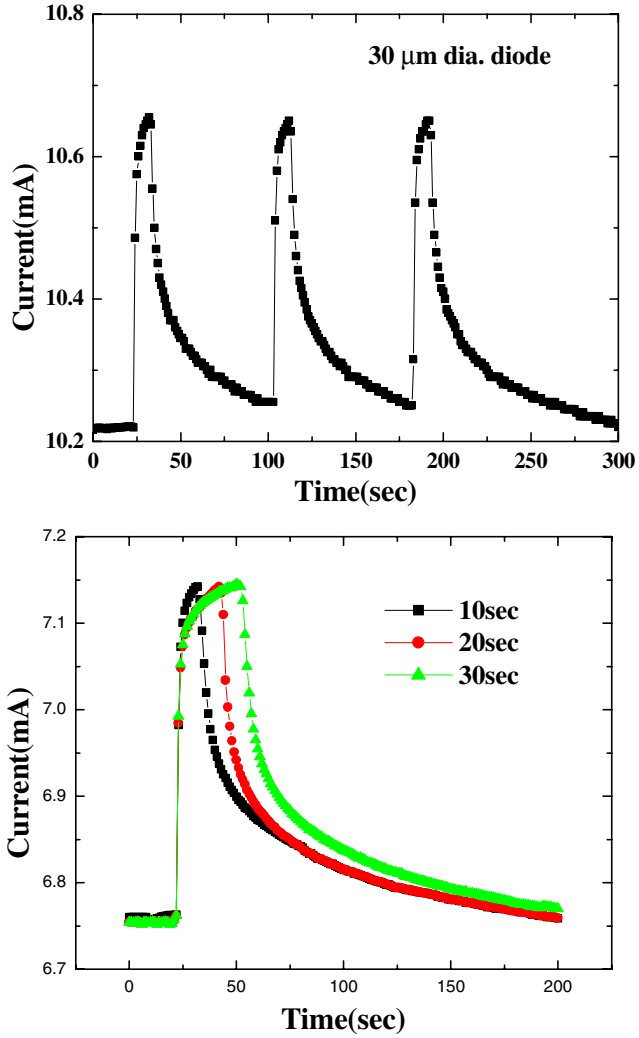

Figure 10. Time response at 25 °C of MOS-HEMT-based diode forward current at a fixed bias of 2 V when switching the ambient from N_2 to 10% H_2/90% N_2 for periods of 10, 20 or 30 s and then back to pure N_2 (bottom) and three cycles of switching the ambient from N_2 to 10% H_2/90% N_2 for periods of 10 (top).

dissociates on the Pt contact and diffuses through the Sc_2O_3 to the interface where it screens some of the piezo-induced channel charge. This is a clear demonstration of the sensitivity of AlGaN/GaN HEMT dc characteristics to the presence of hydrogen in the ambient in which they are being measured. The use of less efficient catalytic metals as the gate metallization would reduce this sensitivity, but operation at elevated temperatures would increase the effect of the hydrogen because of more efficient dissociation on the metal contact.

Figure 11 (right) shows some of the recovery characteristics of the MOS-HEMTs upon cycling the ambient from N_2 to 10% H_2/90% N_2. While the change in drain–source current is almost instantaneous (<1 s), the recovery back to the N_2 ambient value is of the order of 20 s. This is controlled by the mass transport characteristics of the gas out of the test chamber, as

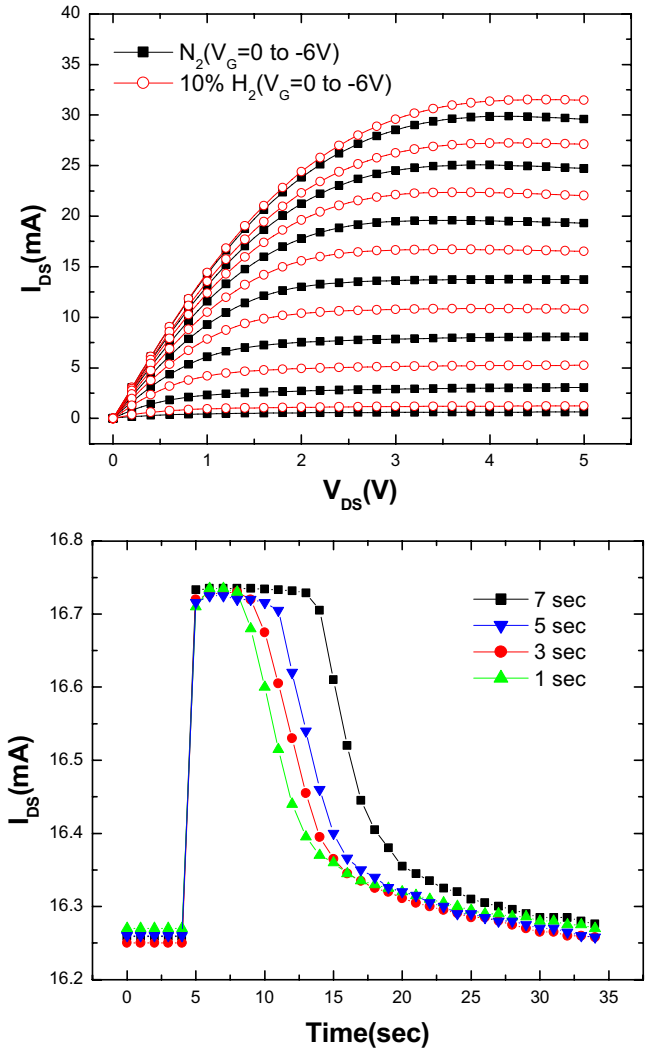

Figure 11. I_{DS}–V_{DS} characteristics of MOS-HEMT measured at 25 °C under pure N_2 ambient or in 10% H_2/90% N_2 ambient (top) and time dependence of drain–source current when switching from N_2 to 10% H_2/90% N_2 ambient and back again for different injection times of the H_2/N_2 (bottom).

demonstrated by changing the total flow rate upon switching the gas into the chamber. Given that the current change upon introduction of the hydrogen is rapid, the effective diffusivity of the atomic hydrogen through the Sc_2O_3 must be greater than 4×10^{-12} cm^2 V^{-1} s^{-1} at 25 °C. Note the complete reversibility of the drain–source current for repeated cycling of the ambient.

Sc_2O_3/AlGaN/GaN MOS-HEMTs show a marked sensitivity of their drain–source current to the presence of hydrogen in the measurement ambient. This effect is due to the dissociation of the molecular hydrogen on the Pt gate contact, followed by diffusion of the atomic species to the oxide/semiconductor interface where it changes the piezo-induced channel charge. The MOS-HEMTs show larger changes in current than their corresponding MOS diode or Schottky diode counterparts and show promise as sensitive hydrogen detectors.

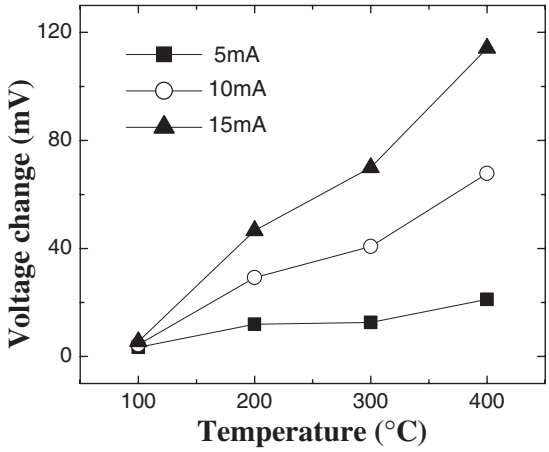

Figure 12. Change in MOS diode forward voltage at fixed currents as a function of temperature for measurement in 100% N_2 or 10% C_2H_4/90% N_2.

Of particular interest are methods for detecting ethylene (C_2H_4), which offers problems because of its strong double bonds and hence the difficulty in dissociating it at modest temperatures. The forward diode current–voltage (I–V) characteristics at 400 °C of the Pt/Sc_2O_3/AlGaN/GaN MOS-HEMT diode both in pure N_2 and in a 10% C_2H_4/90% N_2 atmosphere show that, at a given forward bias, the current increases upon introduction of the C_2H_4. In analogy with the detection of hydrogen in comparable SiC and Si Schottky diodes, a possible mechanism for the current increases involves atomic hydrogen either decomposed from C_2H_4 in the gas phase or chemisorbed on the Pt Schottky contacts then catalytically decomposed to release atomic hydrogen. The hydrogen can then diffuse rapidly though the Pt metallization and the underlying oxide to the interface where it forms a dipole layer [24] and lowers the effective barrier height. We emphasize that other mechanisms could be present; however, the activation energy for the current recovery is ∼1 eV, similar to the value for atomic hydrogen diffusion in GaN [52], which suggests that this is at least a plausible mechanism.

Figure 12 shows the change in voltage at fixed current as a function of temperature for the MOS diodes when switching from a 100% N_2 ambient to 10% C_2H_4/90% N_2. As the detection temperature is increased, the response of the MOS-HEMT diodes increases due to more efficient cracking of the hydrogen on the metal contact. Note that the changes in both current and voltage are quite large and readily detected. In analogy with results for MOS gas sensors in other materials systems [23, 24], the effect of the introduction of the atomic hydrogen into the oxide is to create a dipole layer at the oxide/semiconductor interface that will screen some of the piezo-induced charge in the HEMT channel. The time constant for response of the diodes was determined by the mass transport characteristics of the gas into the volume of the test chamber and was not limited by the response of the MOS diode itself.

Simple Pt or Pd gate GaN Schottky diodes can also provide effective detection of combustion gases. Figure 13 shows a plan view photograph of a two-terminal sensor, along with a device packaged into a header for testing. These devices produce easily measurable changes in forward current upon exposure to hydrogen-containing ambients, as shown in the I–V characteristics of figure 14. These data were taken at 150 °C, but the changes are also measurable at room temperature, showing that the sensors do not need an on-chip heater to increase their detection efficiency, although of course they show larger current changes at higher temperatures.

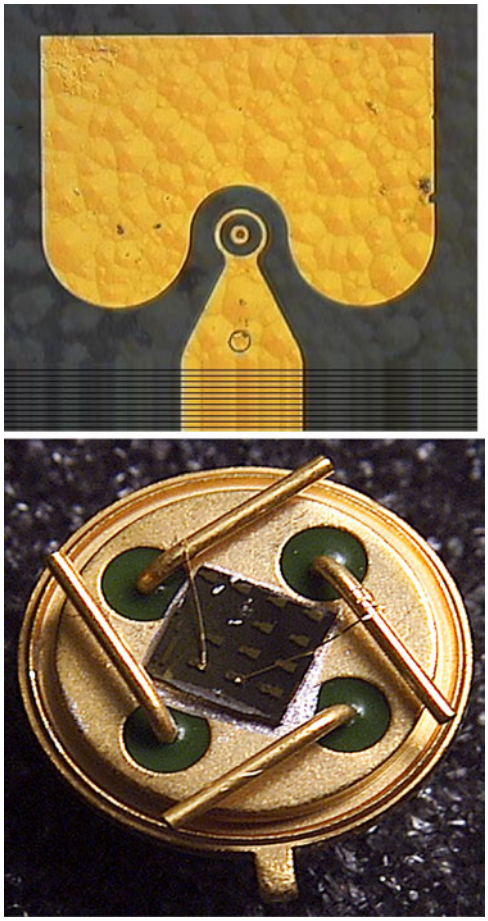

Figure 13. Photographs of two-terminal GaN Schottky diode for gas sensing applications (top) and packaged device (bottom).

2.4. Effect of external strain on conductivity of AlGaN/GaN HEMT

In order to study the effect of external strain on the conductivity of the HEMT, material systems and transmission line patterns were fabricated with a mesa of 500 Å to ensure one-dimensional current flow during the measurement. Figure 15 illustrates the set-up for measuring the effect of external strain on the conductivity of the 2DEG channel of the nitride HEMT. Lucite blocks secure the sample and PCB board for testing. The contact pads were connected to the PCB board, which had BNC connectors on the end for signal outputs, with 1 mil thick gold wire. A high precision single axis traverse was used to bend the sample. The devices were fabricated on half of a 2″ wafer, sawn into 2 mm wide stripes and wire bonded on the test feature, as shown in figure 16. The dc characteristics were obtained from measurements on an Agilent 4156C parameter analyser.

Sheet charges in the AlGaN/GaN high electron mobility transistors (HEMTs) are induced by spontaneous polarization and piezoelectric polarization [51–57]. Wurtzite GaN and AlGaN are tetrahedral semiconductors with a hexagonal Bravais lattice with four atoms per unit cell. The misfit strain inside a film is measured against its relaxed state. In the misfit strain calculation, the strain is calculated against the relaxed films, a_0, i.e.

$$\varepsilon_{\text{misfit}} = \frac{a(x) - a_0(x)}{a_0(x)} \tag{3}$$

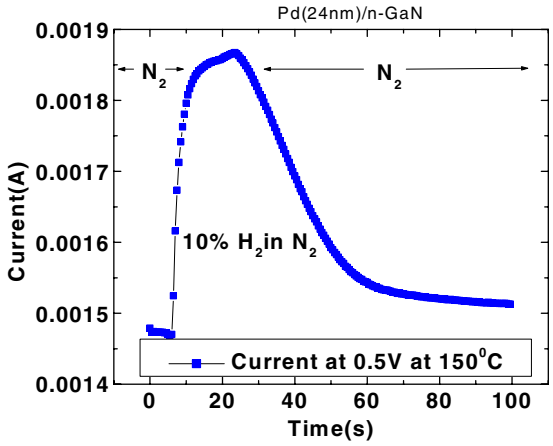

Figure 14. Forward current of Pd/GaN Schottky diode at fixed bias of 0.5 V and a temperature of 150 °C, upon changing the measurement ambient from pure N_2 to 10% H_2 in N_2.

where $a(x)$ is the lattice constants of $Al_xGa_{1-x}N$ and $a_0(x) = (a_{GaN} - a_{AlN}x)$ Å $= (3.189 - 0.077x)$ Å [51]. Here $a(x) - a_0(x)$ is chosen because the AlGaN film is always under tension since $a(x) \leqslant a_{GaN}$ and misfit will always be positive. Having defined the elastic strain in the film, a partially relaxed film parameter should be defined. For a perfectly coherent film, $a(x) = a_{GaN}$ or

$$\varepsilon_{\text{max misfit}} = \frac{a_{GaN} - a_0(x)}{a_0(x)} = \frac{0.077x}{3.189 - 0.077} \approx \frac{0.077x}{3.189} = 0.024x. \tag{4}$$

For a partially relaxed film, the ratio of strain compared to the un-relaxed state defines the degree of strain in the film,

$$S(x) = \frac{\varepsilon_{\text{misft}}}{\varepsilon_{\text{max misfit}}} = \frac{a(x) - a_0(x)}{a_{GaN} - a_0(x)}. \tag{5}$$

Hence, the degree of relaxation is then given by

$$r(x) = 1 - S(x) = \frac{a_{GaN} - a(x)}{a_{GaN} - a_0(x)}. \tag{6}$$

For around 300 Å of AlGaN layer on the top of GaN, $r(x)$ was measured by Ambacher [57].

$$r(x) = \begin{cases} 0 & 0 \leqslant x \leqslant 0.38 \\ 3.5x - 1.33 & 0.38 \leqslant x \leqslant 0.67 \\ 1 & 0.67 \leqslant x \leqslant 1. \end{cases} \tag{7}$$

The piezoelectric polarization, for a partially relaxed strained layer, can be expressed by modifying equation (5) subtracting the portion of relaxation

$$\sigma(x) = 2\,(1 - r(x)) \left(\frac{a_{GaN} - a_0}{a_0} \right) \left(e_{31} - e_{33} \frac{C_{13}}{C_{33}} \right) \tag{8}$$

where e_{31} and e_{33} are the piezoelectric coefficients and C_{13} and C_{33} are the elastic constants.

Figure 17 (bottom) plots the relationship between Al concentration of AlGaN and strain induced by AlGaN on GaN for the un-relaxed and partially relaxed conditions. Unlike the linear model for the un-relaxed condition, there is a maximum strain around an Al concentration of 0.35. The piezoelectric polarization-induced sheet carrier concentration of undoped Ga-face AlGaN/GaN can be calculated from equation (3). As illustrated in figure 17 (top), the

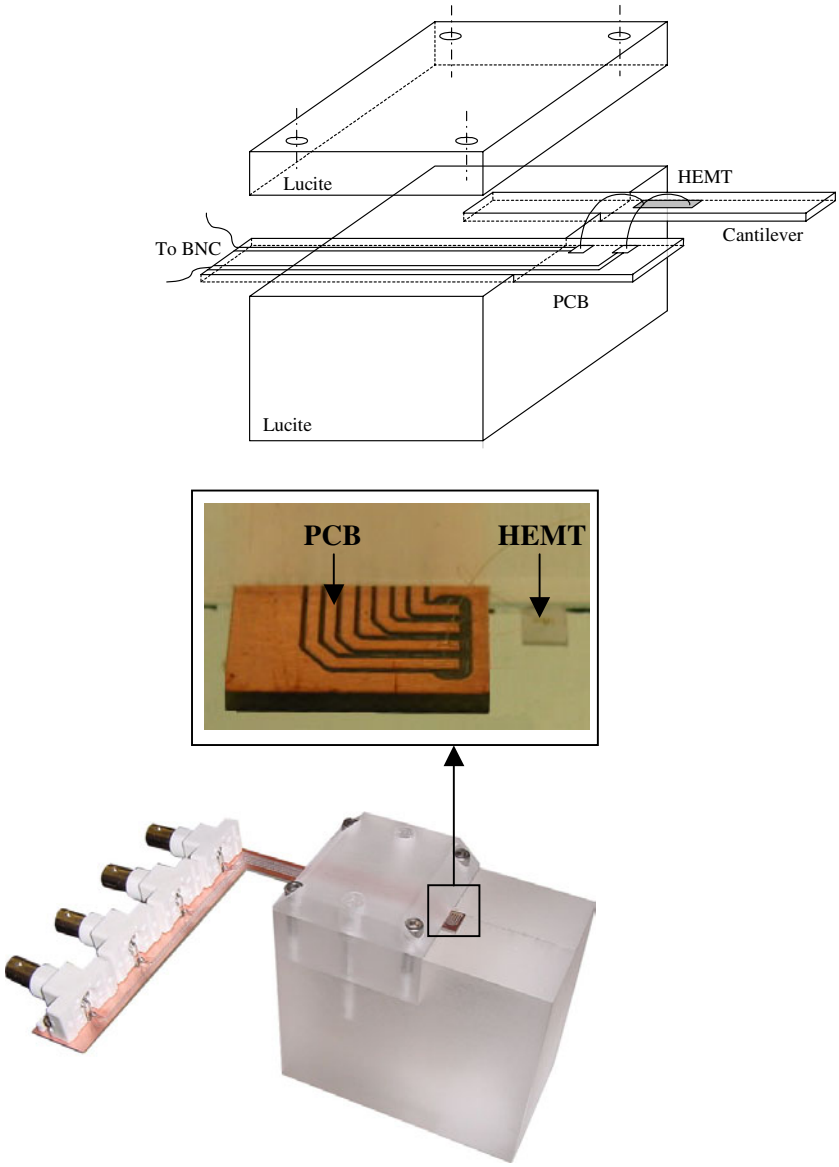

Figure 15. Schematic diagram of a pressure sensor package: experimental set-up to detect I–V characteristics connected to the BNC cable according to various mechanical stresses (top). Picture of actual set-up for cantilever mounting package (bottom).

sheet carrier concentration induced by the piezoelectric polarization is a strong function of Al concentration. In the case of a partially relaxed AlGaN strain layer, there is also a maximum sheet carrier concentration around Al $=$ 0.35. If an external stress can be applied to the AlGaN/GaN material system, the sheet carrier concentration can be changed significantly and devices fabricated in this fashion could be used in sensor-related applications.

A pure bending of a single beam was used in this work to estimate the strain, since the HEMT structure, around 3 μm, is much thinner that that of sapphire substrate, 200 μm, and the

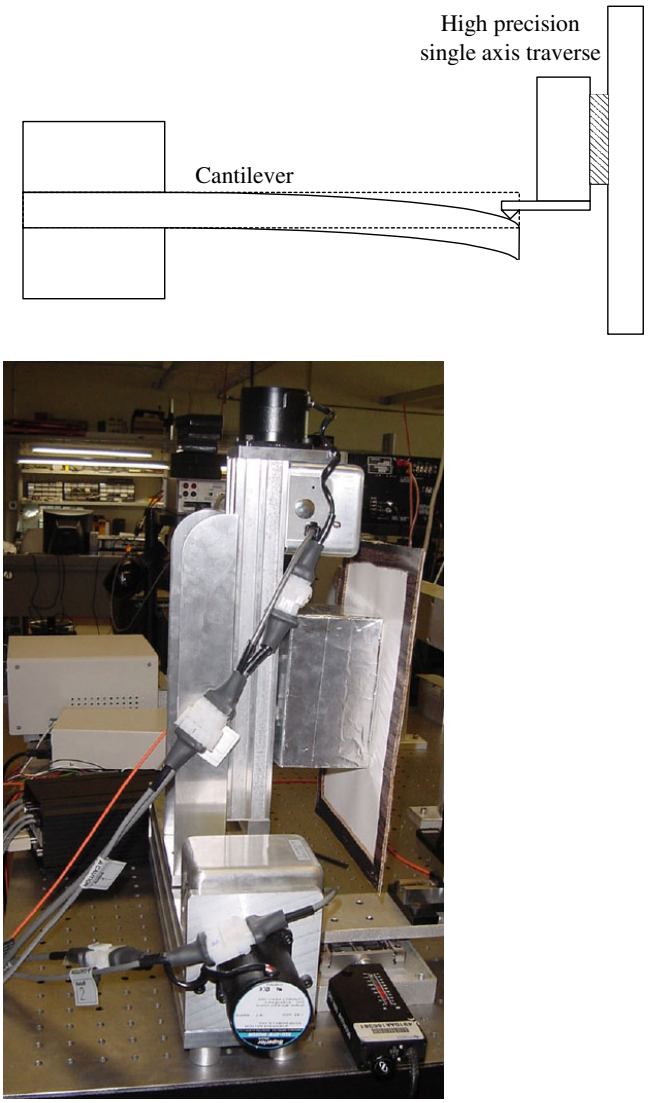

Figure 16. Schematic diagram of mechanical stressor with cantilever (top). Picture of mechanical stressor with high precision single axis traverse (bottom).

degree of deflection (maximum deflection is around 2.2 mm) is much shorter than the length of the beam, 27 mm. The strain, ε_{xx}, of the bending can be estimated from the single beam with thickness of t and unit width. The tensile strain near the top surface of the beam is simply given by [58]

$$\varepsilon_{xx} = td/L^2 \tag{9}$$

where t is the sample thickness, d is the deflection and L is the length of the beam.

Figure 18 shows the effects of external tensile and compressive strain on the conductivity of an AlGaN/GaN HEMT sample with mesa. In the case of applying external tensile strain on the HEMT sample, an increase of conductivity was observed. The mesa depth was around 500 Å, which is below the AlGaN/GaN interface (300 Å AlGaN layer on 3 μm GaN layer).

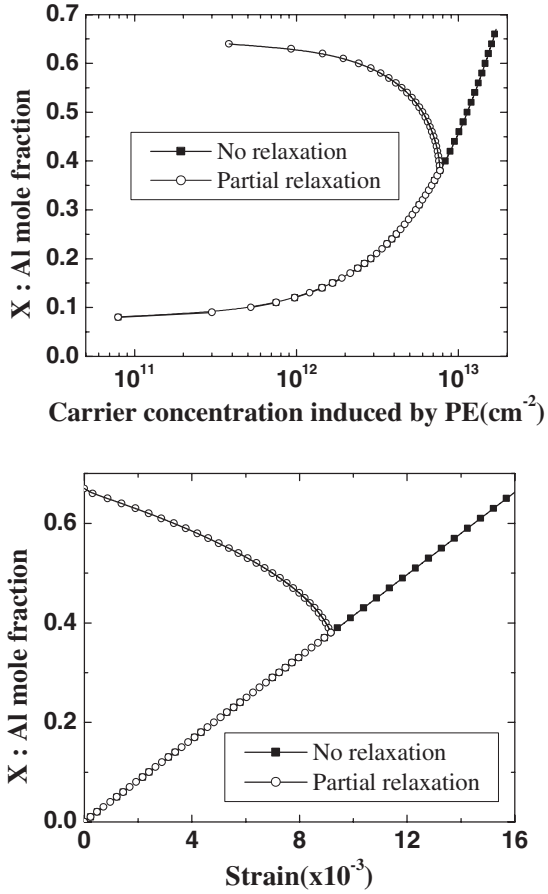

Figure 17. Strain induced by AlGaN on GaN for the un-relaxed and partially relaxed AlGaN layer as a function of Al concentration (bottom) and sheet carrier concentration induced by the piezoelectric polarization as a function of Al concentration (top).

The AlGaN layer is fixed to the GaN underneath and any additional strain generated in the GaN will be replicated in the AlGaN, unless dislocations are generated at the interface. This is the principle of strain gauge measurements. Hence, both layers will be subject to essentially the same change in strain due to bending and any observable difference in the 2DEG density would arise only from differences in the piezo-electric coefficients between GaN and AlGaN. This is sufficiently large that an observable change in conductivity is observed.

2.5. Pressure sensor fabrication

There are at least two approaches that can be taken.

(1) AlGaN/GaN HEMT-based micro-electro-mechanical (MEM) pressure sensors, which can be used at high temperature ambient.

(2) Biosensors with a gateless AlGaN/GaN HEMT membrane, in which the excellent stability of the GaN and AlGaN surface should minimize degradation of adsorbed cells [33].

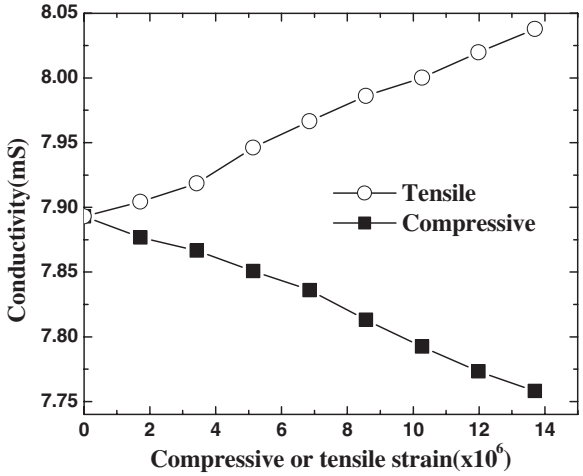

Figure 18. The effect of tensile or compressive stress on the conductivity of mesa-isolated AlGaN/GaN HEMTs.

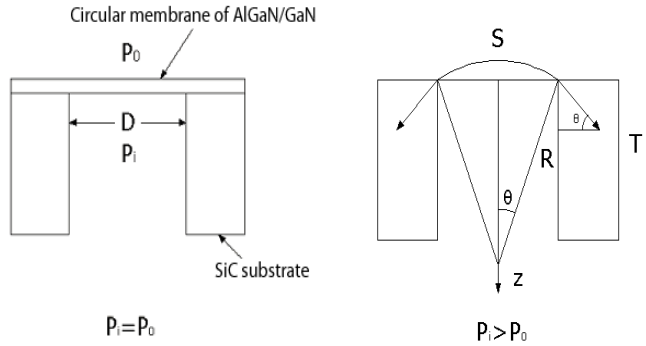

Figure 19. Pressure sensors made of a circular membrane of AlGaN/GaN on a SiC substrate by etching a circular hole in the substrate (left). A deflection of the membrane away from the substrate due to differential pressure on the two sides of the membrane produces a tensile strain in the membrane (right).

The pressure sensors can be made of a circular membrane of AlGaN/GaN on a SiC substrate by etching a circular hole in the substrate, as illustrated in figure 19 (left). A deflection of the membrane away from the substrate due to differential pressure on the two sides of the membrane produces a tensile strain in the membrane, as shown in figure 19 (right). The differential piezoelectric responses of AlGaN and GaN layers create a space charge which induces 2DEG at the AlGaN/GaN interface. The concentration of 2DEG is expected to be directly correlated with the tensile strain in the membrane and hence with the differential pressure. The radial strain is given by [59, 60]

$$\varepsilon_{\mathrm{r}} = (S - D)/D = (2\theta R - 2R\sin\theta)/(2R\sin\theta) = \theta/\sin\theta - 1. \tag{10}$$

The total tensile force around the edge of the circular membrane is [61, 62]

$$T = \pi D t_{\mathrm{GaN}} \sigma_{\mathrm{r}} = \pi D t_{\mathrm{GaN}} [E_{\mathrm{GaN}}/(1-\nu)]\varepsilon_{\mathrm{r}} \tag{11}$$

where t_{GaN} is the film thickness, D is the diameter of the via hole, $\sigma_{\mathrm{r}} = [E_{\mathrm{GaN}}/(1-\nu)]\varepsilon_{\mathrm{r}}$, E_{GaN} is the Young modulus and ν is the Poisson ratio of the GaN film. The component of T along the z direction is balanced by the force on the membrane due to a differential pressure $P_{\mathrm{i}} - P_{\mathrm{o}}$, where P_{i} and P_{o} are the inside and outside pressure respectively.

Hence $T \sin\theta = (P_i - P_o)\pi D^2/4$ and the radial strain, ε_r, in the nitride film can be expressed as a function of the differential pressure $P_i - P_o$.

$$(\theta - \sin\theta) = (P_i - P_o)[(1 - \nu)D]/(4E_{GaN}t_{GaN}) \tag{12}$$

where E_{GaN} is the Young modulus, D is the diameter of the via hole, t_{GaN} is the film thickness and ν is the Poisson ratio of the GaN film. If θ is measured, the differential pressure $P_i - P_o$ can be estimated with equation (12). We also derive the relationship between the conductance, σ, of the AlGaN/GaN HEMT and the radial strain, ε_r [63–65].

$$\sigma = \alpha(r_{AlGaN}) + \beta(f_{GaN}) \times \varepsilon_r \tag{13}$$

where

$$\alpha(r_{AlGaN}) = \mu_s\{1/[1 + (\varepsilon_0\varepsilon(x)/t_{AlGaN}e^2)h^2/4\pi m*(x)]\}\{-|\Delta P_{SP}| - |e_{eff}|\Delta\varepsilon_{AlGaN}r_{AlGaN} - [\varepsilon_0\varepsilon(x)/t_{AlGaN}e][e\phi_b(x) - \Delta E_c(x)]\} \tag{14}$$

and

$$\beta(f_{GaN}) = \mu_s\{1/[1 + (\varepsilon_0\varepsilon(x)/t_{AlGaN}e^2)h^2/4\pi m*(x)]\}\{|e_{eff}(GaN)| - |e_{eff}(AlGaN)|\} \tag{15}$$

μ_s is the mobility of the 2DEG, ε_0 is the electric permittivity, $\varepsilon(x) = 9.5 - 0.5x$ is the relative permittivity, $e\phi_b(x) = 0.84 + 1.3x$ (eV) is the Schottky barrier height, $e_{eff} = (e_{31} - e_{33})C_{13}/C_{33}$, h is the Planck constant, e is the electron charge and $m*(x) \sim 0.228m_e$. By monitoring the conductance of the HEMT on the membrane, the pressure difference, $P_i - P_o$, can be obtained.

Figure 20 illustrates four kinds of potential pressure sensor based on GaN. The first three are based on the conductance measurement to monitor the pressure and the fourth based on the nitride film deflection. Since nitride HEMTs have been demonstrated for wireless communication applications, the pressure sensor can be integrated with wireless circuits. The size of the integrated pressure sensor can be as small as $500 \times 500\ \mu m^2$; the sensor can be placed in pipes or harsh environments for remote sensing.

The first pressure sensor is used to monitor the differential pressure. A via hole can be etched from the back side of the SiC substrate and stop on the front-side GaN layer. The detailed process of via hole formation is described in the next section. Metal electrodes are then deposited on the front side of the membrane and encapsulated with dielectric (SiO_2). Previous demonstrations of W and WSi-based high temperature metal contacts on GaN and SiC, which can be operated at $>800\,^{\circ}C$, suggest that these are good choices for the metallization [66, 67].

In the second design, the via hole of the second sensor is sealed off with another SiC by wafer bonding. The bonding equipment is commercially available. A briefly description of the wafer bonding is in the next section. By seaing off the via hole, the sensor can be used for measurement of the absolute pressure and vacuum, since the via hole seal is performed under atmosphere. In the third sensor, a reference pressure is incorporated, which is not exposed to the high pressure side. Since SiC and GaN are good thermal conductors, the reference will experience the same temperature as the front pressure. A correction of temperature effect on the pressure can be made by subtracting the reference signal from the signal from the front-side pressure sensor. The fourth sensor uses a laser beam to reflect from the back of the nitride membrane to monitor the pressure. With this design, there is no need for metallization on the front side of the sample.

2.6. Selective-area substrate removal

In order to make the AlGaN/GaN MEMS-based membrane, the SiC substrate must be removed in selected areas. As mentioned previously, due to the extremely high chemical stability of

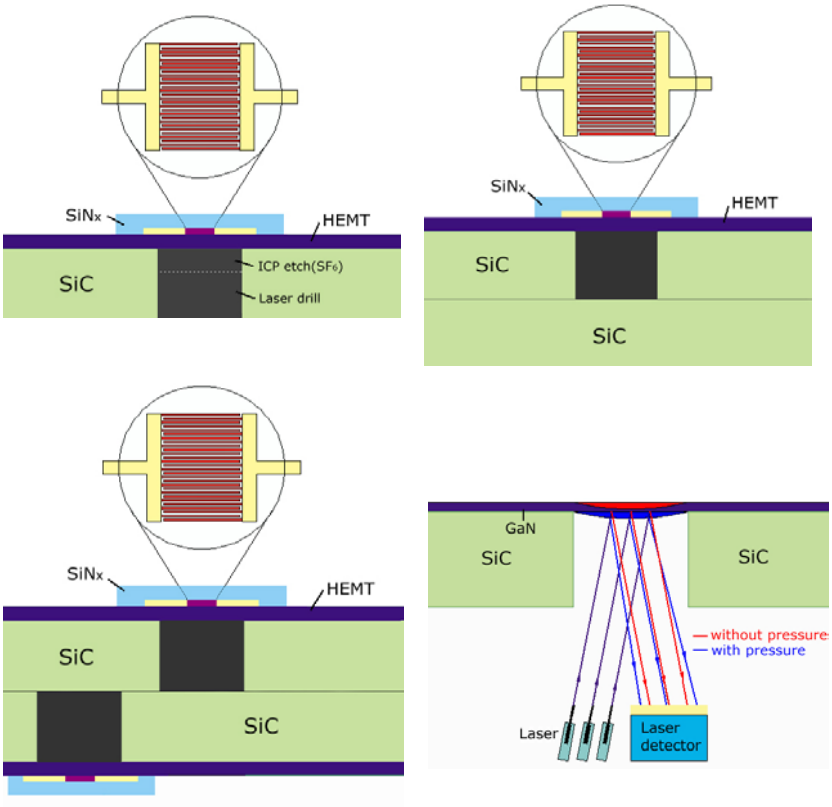

Figure 20. Different designs for GaN-based pressure sensors.

GaN and SiC, there is no convenient wet chemical etchant available. Currently, the etching techniques used for wide bandgap semiconductors are plasma-based dry etching, such as reactive ion etching (RIE), electron cyclotron resonance (ECR) or inductively coupled plasma (ICP) etching [68–79]. Typical etch rates for 4H and 6H SiC substrates in F_2 or Cl_2-based plasmas range between 0.2 and 1.3 μm min^{-1}. Thus even for a thinned-down substrate of 250 μm, the etch time is generally long and as much as 20–80 h under ion energy conditions where mask erosion is not prohibitive. Another significant drawback with dry etching for creating via holes in SiC is the need for a very robust, typically metal, mask material such as Ni, Al or Cr. The deposition, patterning and subsequent removal of such masks adds considerable complexity to the via fabrication process.

Laser drilling is a convenient method to form through-wafer via holes. This technique has been shown to be capable of very high etch rates and precise control of the via size and sidewall slope. Laser drilling is often used to machine hard materials such as super-alloys. A simple model suggests that, above a threshold laser power density, the surface of the material is melted and subsequently ejected by ablation. The development of maskless methods for creating via holes in giant magnetic resistance (GMR) stacks and in particular for standard thickness substrates would give added flexibility for creating custom patterns in the substrates through computer control of the laser drilling location and would also eliminate the need for wafer thinning prior to via formation.

We have obtained the laser ablation rates for SiC in our initial experiments of 229–870 μm min^{-1}, as shown in figure 21 (top).These are significantly faster than the highest

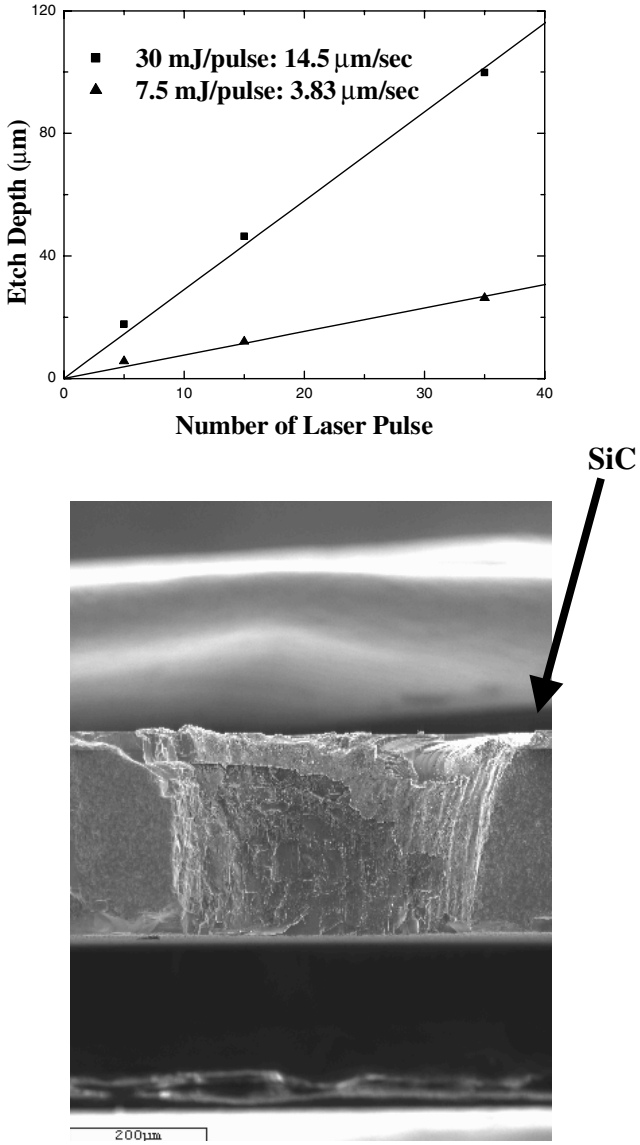

Figure 21. Laser ablation depths in SiC substrates as a function of number of laser pulses. The laser was operated at 5 Hz. An effective etch rate of >200 μm min^{-1} can be achieved (top). Cross sectional view of a 500 μm diameter through-wafer hole on GaN/SiC sample (bottom).

plasma etching rates achieved with ICP etching in F_2-based chemistries. Hence while laser drilling is inherently a serial process when performed in a maskless configuration, the high ablation rates mean that throughput will be comparable to a plasma etch via process in which all the vias are formed simultaneously. A further advantage of the laser drilling technique is that the via hole pattern and the size of the vias can be readily controlled by computer-controlled x–y positioning of the SiC substrate, allowing much more flexibility and reducing costs relative to the need for producing a separate mask in plasma etch processes. We have successfully made laser-drilled vias in materials such as GaN layers grown on SiC substrates,

as shown in figure 21 (bottom). The smallest size of the hole is 20 μm diameter. Since there is no selectivity of laser ablation, we will use laser drilling to remove most of SiC and leave around 20–30 μm SiC. F_2-based selective plasma etching can be employed to etch off the SiC and stop on GaN buffer layer.

2.7. Biosensors using AlGaN/GaN heterostructures

The human immune system is extraordinarily complex, and antigen–antibody interactions are not fully understood at the present time. Antibodies are protein molecules, which are composed of equal numbers of heavy and light polypeptide amino acid chains held together with disulfide bonds. These highly specialized proteins are able to recognize and bind only certain types of antigen molecule at receptor sites. Sensors based on using antibodies to detect certain specific antigens are called immunosensors. These immunosensors are useful for quantifying how well the human immune system is functioning, and could serve as valuable diagnostic tools. They can also be employed for identifying environmental contaminants and chemical or biological agents.

Silicon-based field effect transistors have been widely used as bio-sensors. For example, the silicon-based ion sensitive field effect transistor (ISFET) is already commercialized to replace conventional electrolyte pH metres. Silicon-based metal oxide semiconductor field effect transistors (MOSFETs) and ISFETs have also been used for immunosensors. However, silicon-based FETs are damaged by exposure to solutions containing ions. Si-FET-based biosensors need an ion-sensitive membrane coated over their surface and a reference electrode (usually Ag/AgCl) is required to supply the bias voltage. Special precautions must also be taken to apply those biomembranes over the FETs so that they retain their enzymatic activity. In contrast, GaN-based wide energy bandgap semiconductor material systems are extremely chemically stable. (The only known wet chemical etchant for GaN is molten NaOH at 450 °C.) The bond between Ga and N is ionic and proteins can easily attach to the GaN surface. This is one of the key factors for making a sensitive biosensor with useful lifetime, compared to Si-based FETs requiring coating with a membrane to accomplish this goal.

Ground-breaking work on the selectivity of peptide bonding to semiconductor surfaces has shown that preferential bonding does indeed occur [80–82], and is dependent on a number of factors including crystallographic orientation of the semiconductor surface, ionicity of the semiconductor bonding etc. Previous work has focused primarily on Si, GaAs and InP [80], though studies on metal oxides such as ZnO [81–83] and Cr_2O_3 [84] have also been reported. In most if not all of these cases, detailed understanding of the chemistry behind the observed selectivity has not yet been achieved. Similarly, no information has yet been reported on the effects of the peptide bonding on the underlying characteristics of the semiconductor host. Such information is critical to the development of high sensitivity detection schemes that rely upon changes in the position of the near surface Fermi level for operation.

The development of miniaturized total chemical analysis systems (μTAS) in the past decade is now reflected in the ability of these devices to conduct various chemical and biological analyses in a single chip [85, 86]. There is interest in the development of a microfluidic device for fluid handling and reagent delivery. Such a device will enable the attachment of an array of biomolecules on the surface of GaN FET sensors, for the delivery of a variety of reagents during biological assays, and for simultaneous interrogation of a sample with an array of sensors. The advantages of a microfluidics-based delivery system include the following. First, microfluidics enables highly parallel, high throughput reagent delivery. Miniaturization relieves constraints of real estate challenge when a large number of sensor arrays are exploited. Second, miniaturization enables integration with other components such as electronic circuits

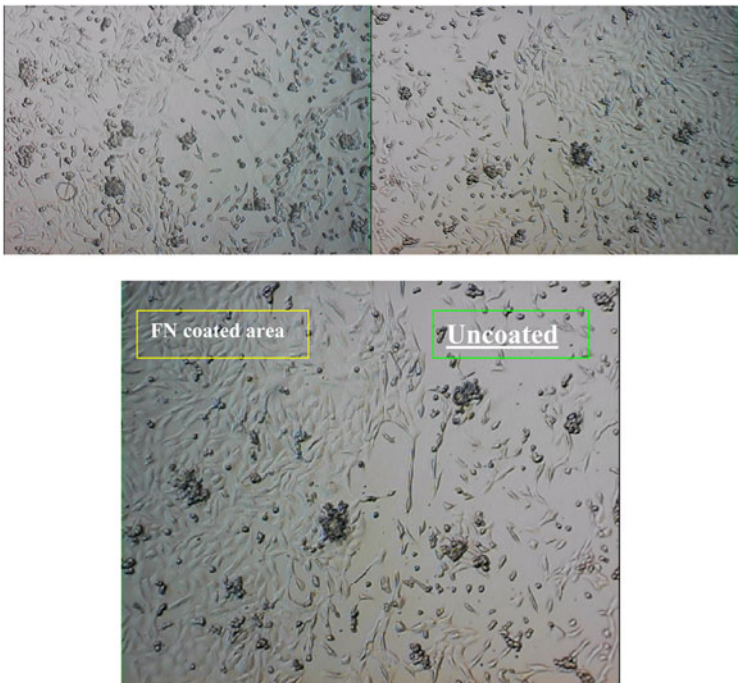

Figure 22. Optical microscope images of V-79 fibroplast cell-coated AlN (left) and GaN (right) surfaces. The image at the bottom shows that providing a nutrient (fibronyacin) to the surface increases the cell density.

and sensing components on the same chip. Therefore the results can be analysed and signal can be interpreted on the device. Third, microfluidics reduces reagent consumption, especially beneficial for very expensive antibodies and enzymes. Other advantages from miniaturization include rapid analysis, ease of automation and potentially low cost.

The chemical sensor array can be integrated with wireless communication circuits for remote sensor applications. This development probably represents assays of the future, which will clearly follow the trend toward increased integration, greater sensitivity, higher specificity and remote sensing. Given the strong sensitivity of gateless HEMT devices to polar materials, there are currently many efforts to use such structures for the detection of ion currents through cell membranes in general and of action potentials of neuron cells in particular. This suggests the possibility of functionalizing the surface for application as biosensors, especially given the excellent stability of the GaN and AlGaN surfaces which should minimize degradation of adsorbed cells. As an example, some initial studies of cell adhesion on GaN and AlN are underway. Figure 22 shows an optical micrograph of V-79 fibroplast cells cultured on AlN and GaN. As suggested by the coating of fibronectin below the cells, they adhere very well to the III nitride surface and survive in a culture medium for a couple of days. So far, very little is known about the interaction of living cell tissue with the III nitride surface, and we are currently performing a systematic investigation of this topic. Eventually it will be necessary to integrate a lipid bilayer membrane onto the surface of the gateless HEMT devices in order to measure single-ion currents associated with high sensitivity bio-detection. A schematic diagram of this approach is shown in figure 23.

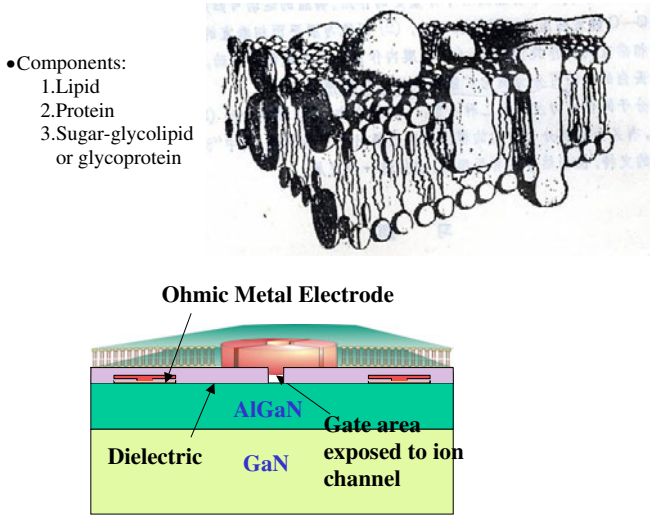

Figure 23. Schematic diagram of lipid bilayer membrane (top) and integration onto the gate region of a AlGaN/GaN HEMT.

2.8. Surface-acoustic-wave- (SAW-) based biosensors

Surface-acoustic-wave- (SAW-) based biosensors for detecting chemical warfare agents, nerve gases and other toxic agents are of interest for the defence industry and homeland security applications. The piezoelectric microbalance or surface acoustic wave transducers can also be used for air sampling, i.e. chemical noses. A neural network type of pattern recognition approach can be incorporated in the design to provide early warning bio-sensor systems which can be built into aircraft and mobile vehicles to detect noxious agents in the external air. Surface acoustic wave (SAW) devices have been successfully used as sensors to detect force, acceleration, shock torque, viscosity, pressure and humidity [87, 88]. SAW devices have also been widely used to monitor thin film thickness and deposition rate during the film deposition. The detection sensitivity is excellent and can detect 0.8% of a monolayer coverage on the surface. By using various coatings on the surface of the SAW devices, various cells, chemicals, gases and bio-materials can be detected [89, 90]. The detection mechanism for the SAW device utilizes the changes to the velocity or phase of an acoustic wave propagating along the substrate due to changes to the characteristics of the propagation path. This is due to the fact that the energy of the surface acoustic wave is stored only in the top region (<1.5 times the wavelength) of the surface of the material in which that wave propagates. Therefore, the surface of a SAW sensor is extremely sensitive to the outer environment. Thus even slight changes in the environment on the surface can be detected. SAWs are not only relatively cheap, very sensitive and reliable, but also do not need a dc-power supply for certain operations, which makes them perfect for wireless applications.

The sensitivity of a SAW device is proportional to the electromechanical coupling coefficients of the substrate. AlN- and GaN-based semiconductor materials are excellent candidates for SAW devices due to their large electromechanical coupling coefficients (similar in magnitude to quartz and much larger than those of GaAs- or SiC-based semiconductors), as illustrated in table 1. GaN HEMTs can be integrated with SAW devices to create a unique acoustic velocity tuning device with low acoustic loss, high frequency and low loss RF performance. The two-dimensional electron gas (2DEG) in the GaN HEMT interacts with the

Table 1. Acoustic velocity and electromechanical coupling coefficient of different SAW materials.

Material	Velocity (m s^{-1})	K^2_{eff}
GaN	3693–4001	0.001 31
AlN	5790	0.002 5
4H-SiC	6832	0.000 112
$LiNbO_3$	3488	0.023 2
GaAs	2867	0.000 593–0.000 64
Quartz	3158	0.001 1
ZnO/R-Al_2O_3	4200	0.06

lateral electric field resulting in Ohmic loss, which attenuates and slows the surface acoustic wave. This mechanism can be used to tune the acoustic velocity. Combined with the optical characteristics of the wide and direct bandgap (∼3.3 eV) semiconductor GaN, the SAW-based chip can also be used for UV optical signal processing. By aligning the device parallel to the *c*-axis of the GaN film, Rayleigh-type SAWs are excluded, while Love-type SAWs are excluded. If the devices are aligned perpendicular to the *c*-axis, the Rayleigh wave mode is suitable for gaseous-type environment sensing. For the Love wave mode operation, there is no vertical wave component, which is ideal for liquid-type environment sensing. The GaN-based SAW chip also offers an acoustic–optical dual-mode sensing mechanism. Likewise, the optical properties parallel and perpendicular to the *c*-axis are different, allowing novel optical devices, such as high contrast modulators. The successful development of the GaN/AlGaN-based HEMT-SAW chip technology will provide industry with state-of-the-art new multifunctional chip technologies. It will not only improve the existing devices but also develop fundamentally new approaches to multi-mode tunable chemical and biochemical sensors.

AlN- and GaN-based material systems are almost ideal SAW materials due to their high SAW velocity, high electromechanical coupling coefficients and compatibility with electronic integration. Nitride-based materials also show excellent resistance to humidity and chemical etching. Nitride-based (AlGaN/GaN) high electron mobility transistors have shown a strong piezoelectric effect and have been used to fabricate very sensitive piezoelectric microbalances. Biologically active films can be coated on the microbalance. Microbalances and the influence of adsorption of toxicants and rate of toxicant mass accumulation can affect the acoustic waves propagating in the AlGaN/GaN layer. The high electromechanical coupling coefficients of piezoelectric nitride-based materials in conjunction with the properties of low acoustic loss and high velocity offer excellent potential for use in high frequency and low loss RF applications. SAW devices operating in the kHz to GHz range can be designed and integrated with wireless remote sensing applications.

The GaN-based SAW chip also offers an acoustic–optical dual-mode sensing mechanism. Likewise, the optical properties parallel and perpendicular to the *c*-axis are different, allowing novel optical devices, such as high contrast modulators. It is highly desirable to increase the device operation frequency of SAW devices as this has been shown to improve the signal-to-noise ratio and the detectivity of such devices [91]. Operation frequency is a function of the device size, determined by lithography, and the velocity of propagation in the SAW media. Conventional piezoelectric materials, such as quartz or lithium niobate, offer limited performance due to their relatively low velocities of ∼3000 $\simeq$ 4000 m s^{-1} [92]. Thin piezoelectric films which have high SAW velocity and which can be integrated with a non-piezoelectric substrate such as Si are highly desirable. AlN is an almost ideal SAW material due to its high SAW velocity, ∼5600 m s^{-1}, as illustrated in table 1, and its compatibility with electronic integration [93–98]. AlN on Si is a particularly attractive combination as the

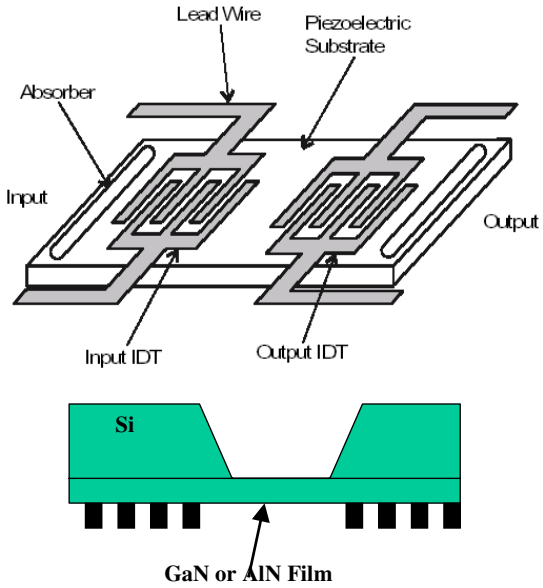

Figure 24. Schematic diagrams of inter-digital-transducer- (IDT-) based SAW (top) and flexural plate wave SAW (bottom) devices.

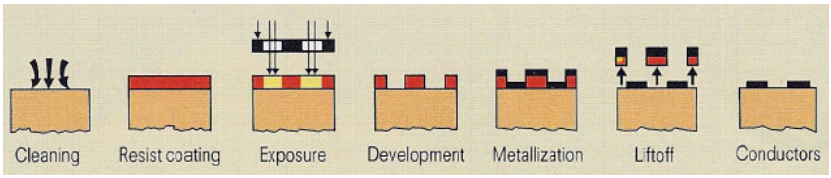

Figure 25. Fabrication sequence of the inter-digital transducer (IDT).

opposite temperature coefficients of delay of Si and AlN facilitate realization of thermally stable SAW devices. Preliminary work on this material system reported in the literature has shown great promise [98]. This work was carried out using sputtering to deposit the AlN. The resultant microstructure was fine grained and poly-crystalline. Significant improvement is expected if higher quality films are employed. This can be achieved by using epitaxial processes, such as molecular beam epitaxy (MBE).

2.9. Surface acoustic wave device fabrication

Both inter-digitated-transducer- (IDT-) based SAW and flexural plate wave SAW devices can be employed for sensing gas or liquid bio-agents, respectively, as illustrated in figure 24. For both kinds of SAW device, a pair of IDTs is fabricated on the substrate (AlN or GaN) as the input and output port of the signals. The fabrication of SAW devices consists of material selection, photolithography, metal deposition, dicing and chip-mounting as depicted in figure 25.

The SAW devices are designed according to the frequency and bandwidth of operation. The acoustic wave can be expressed as a complex constant ($\gamma = \alpha + j\beta$). The attenuation constant, α, and propagation constant, $\beta = 2\pi/\lambda$, are important design parameters of the SAWs, where λ is the acoustic wavelength. Another important design parameter is the

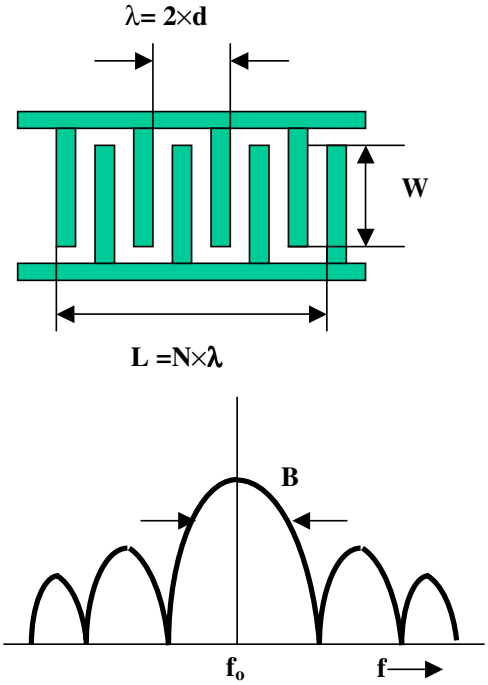

Figure 26. The dimension of the SAW device depends on the operation frequency of the SAW (top). The bandwidth of the SAW is a function of the number of the IDT and the frequency (bottom).

electromechanical coupling coefficient, K^2, which is a measure of the efficiency in converting an applied microwave signal into mechanical energy. These parameters will determine the magnitude of the observed changes in the SAW phase velocity, $\Delta v/v$, and attenuation of the SAW intensity, Γ, and can be expressed as

$$\Gamma = \frac{K^2}{2}\frac{2\pi}{\lambda}\frac{\sigma/\sigma_{\mathrm{m}}}{1+(\sigma/\sigma_{\mathrm{m}})^2} \tag{16}$$

and

$$\frac{\Delta v}{v} = \frac{K^2}{2}\frac{1}{1+(\frac{\sigma}{\sigma_{\mathrm{m}}})^2} \tag{17}$$

where σ is the sheet conductivity and σ_{m} is the critical conductivity at which maximum attenuation occurs.

The physical SAW devices can be designed by choosing the desired operating frequency and bandwidth. As illustrated in figure 26 (top), the operation frequency of the SAW device, f_{o}, can be designed by properly choosing the spacing between the inter-digital fingers, d, such that

$$f_{\mathrm{o}} = \frac{v}{d} \tag{18}$$

where v is the wave velocity in the specific substrate. Therefore, the dimensions of the SAW devices depend on the operation frequency, which can vary from a few microns for GHz operation to mm range for kHz operation. SAW devices operating in the kHz to GHz range

Table 2. Coatings for surface acoustic wave devices.

Analyte	Coating	Detection limit
Explosive	Carbowax 1000	1 ppb
Sulfur dioxide	Dinonyl phthalate	5 ppm
Toluene	Polyamidoxime	90 ppm
Phosgene	Methyltrioctyl phosphonium dimethylphosphate	5 μg l^{-1}
H_2	Pd	50 ppm
Hg	Au	2×10^{-3} M
H_2S	WO_3	10 ppb
NH_3	Pt	1 μg ml^{-1}
NO_2	MnO_2	7 ppm
SO_2	Au	20 ppb
Ozone	Polybutadiene	10 ppb
Candida albicans	Anti-candida antibody	10^6 cells cm^{-1}
Glucose	Hexokinase	1 mM
Human IgG	Goat antihuman IgG protein A	12 μg

can be readily designed and integrated with RF integrated circuits for wireless remote sensing applications. The bandwidth of the acoustic wave is given as

$$B = \frac{v}{2 \times N \times d} \tag{19}$$

where N is the number of inter-digital fingers, as shown in figure 26 (bottom).

2.10. Surface acoustic wave device for gas sensing

Gas sensing is achieved by producing a change in the characteristics of the substrate material between the input and output IDTs, where the acoustic waves travel. A pair of SAW devices can be used for gas sensing; one as the reference and the other for detection. Depending on the type of chemical and bio-agent needing to be detected, an absorbing layer for the specific chemical or bio-agent is coated on the surface of the SAW between the input and output IDTs. Initially two sets of SAWs are impedance-matched, which means the wave reaching the output IDT will have the same phase and the same velocity. If the bio-agents adhere to the coated materials, the phase of the wave will be affected by the bio-agents, then these two sets will have different phases. By integration with a mixer, one can monitor the change easily. Table 2 contains a list of coatings for specific chemical agents. Excellent gas detection should be observed for GaN- and AlN-based SAW devices.

2.11. Flexural plate wave (FPW) device for liquid sensing

As shown in figure 24 (right), the configuration of the FPW is identical to the gas-sensing-based SAW device, with the exception of an additional via hole fabricated on the substrate to accommodate the liquid sample. GaN membranes can be fabricated by etching off the Si substrate in an inductively coupled plasma (ICP) system using SF_6-based chemistry. Thick photoresist (>10 μm) is used as the etch mask.

2.12. SAW array

To increase selectivity, it is typical to employ an array of SAW devices, with different coatings used to identify specific chemicals or bio-agents. Since each SAW device is so small, the arrays

are portable. In addition, integrated with a power amplifier such as a microwave monolithic integrated circuit (MMIC), these devices can be transported by an unmanned aircraft into dangerous environments. SAW devices do not need a power supply, so once they are installed at targeted areas, they can be monitored wirelessly without a battery, which means they can operate semi-permanently. The successful development of the GaN/AlGaN based HEMT-SAW chip technology will provide industry with state-of-the-art new multifunctional chip technologies. It will not only improve the existing devices but also develop fundamentally new approaches to multi-mode tunable chemical and biochemical sensors.

2.13. Wireless sensor network and wireless sensor array using RFID technology

Due to their flexibility in field deployment, sensors with wireless data transmission capability are of great interest for applications in security, civil engineering, biometrics, telemedicine, homeland defence, transportation, etc. For many applications, multiple wireless sensors of the same function or different functions need to be deployed at multiple locations. A simple wireless sensor network is therefore needed to manage the collection and process of data from multiple sensors at multiple locations. It is preferable to make the RF transceiver in each wireless sensor as simple as possible to reduce its size and power consumption.

The radio frequency identification (RFID) technology has advanced to a level where an ultra-small RFID tag can be monolithically integrated in a tiny chip. The tag device consumes very little power and therefore can operate with a very small battery or even without battery. In the latter case, the tag device is powered by the external interrogation signal from the base station. Its low data bandwidth, low power operation made it suitable to integrate with sensors for wireless sensing, since the data bandwidth and operating power of the sensor is also very low. Once the detected sensor data are digitized, they can be merged with the ID code and transmitted together. The RFID part of the integrated wireless sensor functions as a simple RF transceiver which receives base station signal to turn on the transmitter and sends back the sensor data. This type of wireless sensor is suitable for short range operation similar to a personal area network (PAN).

It is possible to combine sensor technologies and RFID technologies to build a simple wireless sensor network. The network consists of multiple sensors of the same function or different functions, e.g., chemical, biological agent, pressure, temperature and UV detections. Each sensor is connected to an RFID tag with a unique ID code that identifies its sensing function and location. Two operation modes, active and passive, will be studied. In the active operation mode, it sends out the data to a central monitor station whenever the sensor detection is positive and triggers the RFID tag transmitter. A battery or other power source is needed to operate the wireless sensor. In the passive operation mode, the sensor is activated by the central monitor station's interrogation signal and responds with the data. Extremely low power wireless sensor design will be explored to investigate the feasibility of powering the device with an RF interrogation signal, which eliminates the need to use a battery. Figure 27 shows the block diagram of the integrated wireless sensor with RFID. The sensor can be powered by the external interrogation RF energy from base station, or an integrated battery. The sensor data is merged with the RFID code, which modulates the antenna load and the reflected signal from the base station.

A wireless sensor array using RFID is similar to the above except that multiple wireless sensors are integrated together on one substrate. A typical example is a biomedical or biochemical lab-on-chip. Two types of integration can be employed, hybrid integration and monolithic integration. In hybrid integration, an array of wireless sensors, with each consisting of a printed antenna, an RF tag circuit and a sensor, will be integrated on a PCB substrate. The

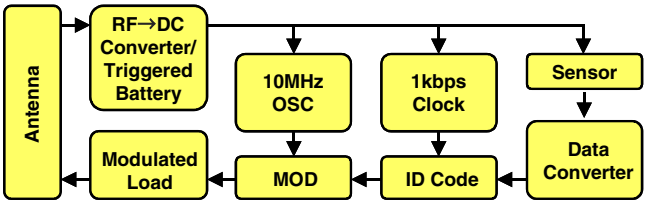

Figure 27. Block diagram of wireless sensor with RFID.

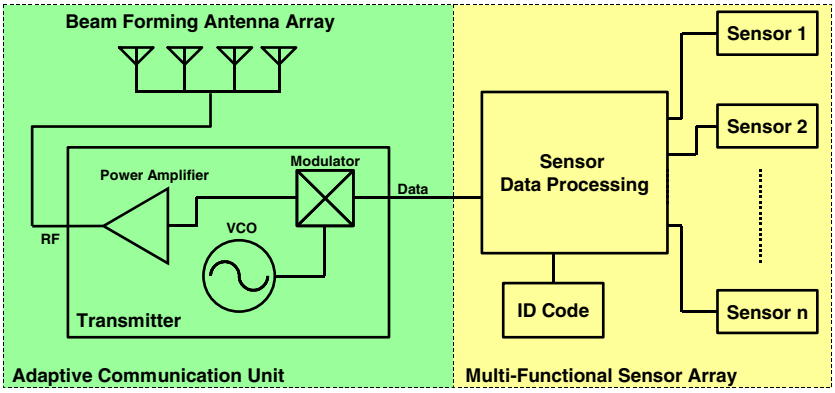

Figure 28. Long range wireless sensor.

antenna size is dominant and determines the overall size of the wireless sensor array. To have monolithic integration, the antenna needs to be small and operating at higher frequency.

The advantages of using RFID technology are small size, low cost, and low power. On the other hand, the RFID technology is limited in range, which is in the order of a few metres. For some applications where size and power consumption are not critical, but operating distance is a major concern, the wireless sensor architecture in figure 28 can be used. The device consists of multiple sensors, a memory that stores its ID code, a data processor that collects sensor data and merges with the ID code and a transmitter with power amplifier and antenna array for long range transmission. The beam-forming antenna array can be pre-programmed to point the antenna beam to the central station.

Finally, it is possible to use the signals from a distributed sensor array to track the extent of a gas or chemical release in real time. Figure 29 shows a simulation of the spreading of a gas release in an urban environment (the white shapes represent buildings) by combining wind speeds and directions, ambient temperature, nature of the gas etc. A distributed network of GaN-based sensors with integrated wireless data transmission would be capable of real-time tracking of the extent of chemical contamination.

3. Summary

We have demonstrated that AlGaN/GaN HEMTs show a strong dependence of source/drain current in piezoelectric polarization-induced 2DEGs on variations in electrostatic boundary conditions of the free surface above the 2DEG (polar liquids, decomposition of hydrogen by catalytic Pt contacts and applied strain). These particularly attractive features of AlGaN/GaN heterostructure makes it possible for these sensors to function in principle with excellent

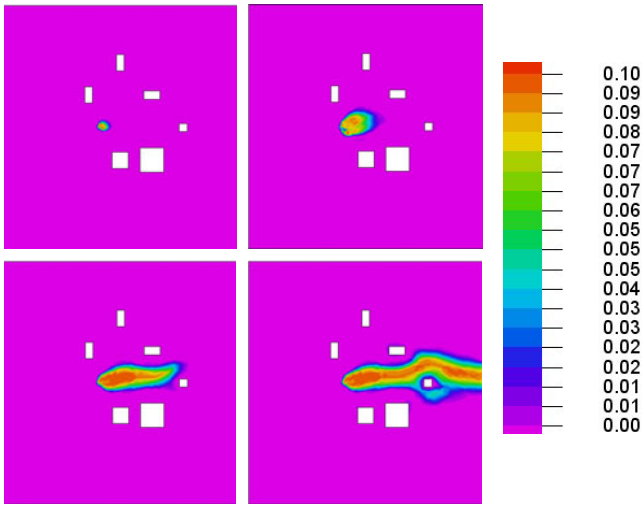

Figure 29. Simulation of time dependence of spreading of a gas release between buildings.

thermal, chemical and mechanical stability, which suggests that nitride HEMTs are excellent candidates for pressure sensor and piezoelectric-related applications. Much more research is needed to develop AlGaN/GaN heterostructure-based sensors which really can compete in real applications.

Acknowledgments

The work at UF is partially supported by AFOSR (F49620-02-1-0366, G Witt and F49620-03-1-0370), NSF (CTS-0301178, monitored by Drs M Burka and D Senich), NASA Kennedy Space Center grant NAG 10-316 monitored by Mr Daniel E Fitch, ONR (N00014-98-1-02-04, H B Dietrich) and NSF DMR 0101438. We appreciate the contributions of A El Kouche, K Ip, D P Norton, K H Baik, M E Law and R Fox to this work.

References

[1] see for example, Eastman L F and Mishra U K 2002 *IEEE Spectr.* **39** 28
[2] Tarakji A, Hu X, Koudymov A, Simin G, Yang J, Khan M A, Shur M S and Gaska R 2002 *Solid-State Electron.* **46** 1211
[3] Koudymov A, Hu X, Simin K, Simin G, Ali M, Yang J and Khan M A 2002 *IEEE Electron. Device Lett.* **23** 449
[4] Simin G, Koudymov A, Fatima H, Zhang J P, Yang J, Khan M A, Hu X, Tarakji A, Gaska R and Shur M S 2002 *IEEE Electron. Device Lett.* **23** 458
[5] Eastman L F *et al* 2001 *IEEE Trans. Electron Devices* **48** 479
[6] Johnson J W *et al* 2001 *Solid-State Electron.* **45** 1979
[7] Lu W, Yang J, Khan M A and Adesida I 2001 *IEEE Trans. Electron Devices* **48** 581
[8] Pearton S J, Ren F, Zhang A P and Lee K P 2000 *Mater. Sci. Eng.* R **30** 55
[9] Binari S C, Ikossi K, Roussos J A, Kruppa W, Park D, Dietrich H B, Koleske D D, Wickenden A E and Henry R L 2001 *IEEE Trans. Electron Devices* **48** 465
[10] Simin G, Koudymov A, Tarakji A, Hu X, Yang J, Asif Khan M, Shur M S and Gaska R 2001 *Appl. Phys. Lett.* **79** 2651
[11] Lloyd Spetz A, Baranzahi A, Tobias P and Lundström I 1997 *Phys. Status Solidi* a **162** 493
[12] Vasiliev A, Moritz W, Fillipov V, Bartholomäus L, Terentjev A and Gabusjan T 1998 *Sensors Actuators* B **49** 133

[13] Savage S M, Konstantinov A, Saroukan A M and Harris C 2000 *Proc. ICSCRM '99* pp 511–5
[14] Lloyd Spetz A, Tobias P, Unéus L, Svenningstorp H, Ekedahl L-G and Lundström I 2000 *Sensors Actuators* B **70** 67
[15] Connolly E J, O'Halloran G M, Pham H T M, Sarro P M and French P J 2002 *Sensors Actuators* A **99** 25
[16] Arbab A, Spetz A and Lundström I 1993 *Sensors Actuators* B **15/16** 19
[17] Hunter G W, Neudeck P G, Okojie R S, Beheim G M, Thomas V, Chen L, Lukco D, Liu C C, Ward B and Makel D 2002 *Proc. ECS* **1/2** 212
[18] Chen L Y, Hunter G W, Neudeck P G, Knight D L, Liu C C and Wu Q H 1996 *Proc. 3rd Int. Symp. on Ceramic Sensors* ed H U Anderson, M Liu and N Yamazoe (Pennington, NJ: Electrochemical Society) pp 92–8
[19] Ekedahl L-G, Eriksson M and Lundstrom I 1998 *Acc. Chem. Res.* **31** 249
[20] Svenningstorp H, Tobias P, Lundström I, Salomonsson P, Mårtensson P, Ekedahl L-G and Spetz A L 1999 *Mater. Sci. Eng.* B **57** 159
[21] Hunter G W, Liu C C and Makel D 2001 *MEMS Handbook* ed M G Hak (Boca Raton, FL: CRC Press)
[22] Chen L, Hunter G W and Neudeck P G 1997 *J. Vac. Sci. Technol.* A **15** 1228
Chen L, Hunter G W and Neudeck P G 1998 *J. Vac. Sci. Technol.* A **16** 2890
[23] Tobias P, Baranzahi A, Spetz A L, Kordina O, Janzen E and Lundstrom I 1997 *IEEE Electron. Device Lett.* **18** 287
[24] Baranzahi A, Lloyd Spetz A and Lundström I 1995 *Appl. Phys. Lett.* **67** 3203
[25] Casady J B, Agarwal A K, Seshadri S, Siergiej R R, Rowland L B, MacMillan M F, Sheridan D C, Sanger P A and Brandt C D 1998 *Solid-State Electron.* **42** 2165
[26] Ambacher O *et al* 2002 *Proc. ECS* **214** 27
[27] Neuberger R, Muller G, Ambacher O and Stutzmann M 2001 *Phys. Status Solidi* a **185** 85
[28] Schalwig J, Muller G, Ambacher O and Stutzmann M 2001 *Phys. Status Solidi* a **185** 39
[29] Steinhoff G, Hermann M, Schaff W J, Eastmann L F, Stutzmann M and Eickhoff M 2003 *Appl. Phys. Lett.* **83** 177
[30] Eickhoff M, Neuberger R, Steinhoff G, Ambacher O, Muller G and Stutzmann M 2001 *Phys. Status Solidi* b **228** 519
[31] Schalwig J, Muller G, Eickhoff M, Ambacher O and Stutzmann M 2002 *Sensors Actuators* B **81** 425
[32] Stutzmann M *et al* 2002 *Diamond Relat. Mater.* **11** 886
[33] Eickhoff M *et al* 2003 *Phys. Status Solidi* c **6** 1908
[34] Kim J, Gila B, Chung G Y, Abernathy C R, Pearton S J and Ren F 2003 *Solid-State Electron.* **47** 1069
[35] Kim J, Ren F, Gila B, Abernathy C R and Pearton S J 2003 *Appl. Phys. Lett.* **82** 739
[36] Kim J, Gila B, Abernathy C R, Chung G Y, Ren F and Pearton S J 2003 *Solid-State Electron.* **47** 1487
[37] Ambacher O, Eickhoff M, Link A, Hermann M, Stutzmann M, Bernardini F, Tilak V and Eastmann L F 2003 *Phys. Status Solidi* c **6** 1878
[38] Khan M A, Hu X, Simin G, Lunev A, Yang J, Gaska R and Shur M S 2001 *IEEE Electron. Device Lett.* **21** 63
[39] Kang B S, Louche G, Duran R S, Gannou Y, Pearton S J and Ren F 2004 *Solid-State Electron.* **48** 851
[40] Kang B S *et al* 2003 *Appl. Phys. Lett.* **83** 4845
[41] Zhang A P, Rowland L B, Kaminsky E B, Tilak V, Grande J C, Teetsov J, Vertiatchikh A and Eastman L F 2003 *J. Electron. Mater.* **32** 388
[42] Morkoc H, Cingolani R and Gil B 1999 *Solid-State Electron.* **43** 1909
[43] Shur M S 1990 *Physics of Semiconductor Devices* (Englewood Cliffs, NJ: Prentice-Hall)
[44] Pala N, Gaska R, Rumyantsev S, Shur M S, Asif Khan M, Hu X, Simin G and Yang J 2000 *Electron. Lett.* **36** 268
[45] Simin G, Hu X, Ilinskaya N, Kumar A, Koudymov A, Zhang J, Asif Khan M, Gaska R and Shur M S 2000 *Electron. Lett.* **36** 2043
[46] Tarakji A, Hu X, Koudymov A, Simin G, Yang J, Khan M A, Shur M S and Gaska R 2002 *Solid-State Electron.* **46** 1211
[47] Koudymov A, Hu X, Simin K, Simin G, Ali M, Yang J and Khan M A 2002 *IEEE Electron. Device Lett.* **23** 449
[48] Simin G, Koudymov A, Fatima H, Zhang J P, Yang J, Khan M A, Hu X, Tarakji A, Gaska R and Shur M S 2002 *IEEE Electron. Device Lett.* **23** 458
[49] Gila B P, Johnson J W, Mehandru R, Luo B, Onstine A H, Krishnamoorthy V, Bates S, Abernathy C R, Ren F and Pearton S J 2001 *Phys. Status Solidi* a **188** 239
[50] Kim J, Mehandru R, Luo B, Ren F, Gila B P, Onstine A H, Abernathy C R, Pearton S J and Irokawa Y 2000 *Appl. Phys. Lett.* **80** 4555
[51] Kim J, Mehandru R, Luo B, Ren F, Gila B P, Onstine A H, Abernathy C R, Pearton S J and Irokawa Y 2000 *Appl. Phys. Lett.* **81** 373
[52] Pearton S J, Zolper J C, Shul R J and Ren F 1999 *J. Appl. Phys.* **86** 1

[53] Green B M, Chu K K, Chumbes E M, Smart J A, Shealy J R and Eastman L F 2000 *IEEE Electron. Device Lett.* **21** 268
[54] Tarakji A, Hu X, Koudymov A, Simin G, Yang J, Khan M A, Shur M S and Gaska R 2002 *Solid-State Electron.* **46** 1211
[55] Zhang A P, Rowland L B, Kaminsky E B, Tilak V, Grande J C, Teetsov J, Vertiatchikh A and Eastman L F 2003 *J. Electron. Mater.* **32** 388
[56] Koudymov A, Hu X, Simin K, Simin G, Ali M, Yang J and Khan M A 2002 *IEEE Electron. Device Lett.* **23** 449
[57] Ambacher O *et al* 2000 *J. Appl. Phys.* **87** 334
[58] Rashmi H, Kranti A, Haldar S and Gupta R S 2002 *Microelectron. J.* **33** 205
[59] Chen W Q and Hark S K 1995 *J. Appl. Phys.* **77** 5747
[60] Neuberger R, Muller G, Ambacher O and Stutzmann M 2001 *Phys. Status Solidi* a **185** 85
[61] Ambacher O *et al* 1999 *J. Appl. Phys.* **85** 3222
[62] Asbeck P M, Yu E T, Lau S S, Sullivan G J, Van Hove J and Redwing J M 1997 *Electron. Lett.* **33** 1230
[63] Stoney G G 1909 *Proc. R. Soc.* **82** 172
[64] Chu S N G 1998 *J. Electrochem. Soc.* **145** 3621
[65] *CRC Handbook of Chemistry and Physics* 1997 77th edn (New York: CRC press)
[66] Kim J, Ren F, Baca A G, Briggs R D and Pearton S J 2003 *Solid-State Electron.* **47** 1345
[67] Kim J, Ren F, Baca A G and Pearton S J 2003 *Appl. Phys. Lett.* **82** 3263
[68] Yih P H and Steckl A J 1995 *J. Electrochem. Soc.* **142** 2853
[69] Leerungnawarat P, Hays D C, Cho H, Pearton S J, Strong R M, Zetterling C-M and Östling M 1999 *J. Vac. Sci. Technol.* B **17** 2050
[70] Tanaka S, Rajanna K, Abe T and Esashi M 2001 *J. Vac. Sci. Technol.* B **19** 2173
[71] Li B, Cao L and Zhao J H 1998 *Appl. Phys. Lett.* **73** 653
[72] Flemish J R, Xie K and Zhao J H 1994 *Appl. Phys. Lett.* **64** 2315
[73] Khan F A and Adesida I 1999 *Appl. Phys. Lett.* **75** 2268
[74] Cho H, Leerungnawarat P, Hays D C, Pearton S J, Chu S N G, Strong R M, Zetterling C-M, Östling M and Ren F 2000 *Appl. Phys. Lett.* **76** 739
[75] Chabert P, Proust N, Perrin J and Boswell R W 2000 *Appl. Phys. Lett.* **76** 2310
[76] Wang J J, Lambers E S, Pearton S J, Ostling M, Zetterling C-M, Grow J M, Ren F and Shul R J 1998 *J. Vac. Sci. Technol.* A **16** 2204
[77] McLane G F and Flemish J R 1996 *Appl. Phys. Lett.* **68** 3755
[78] Khan F A, Zhou L and Kumar V 2002 *J. Electrochem. Soc.* **149** G420
[79] Leerungnawarat P, Lee K P, Pearton S J, Ren F and Chu S N G 2001 *J. Electron. Mater.* **30** 202
[80] Whaley S R, English D S, Hu E L, Barbara P F and Belcher A M 2000 *Nature* **405** 665
[81] Nguyen C, Dai J, Darikaya M, Schwartz D T and Baneyx F 2003 *J. Am. Chem. Soc.* **43** 256
[82] Sarikaya M, Tamerler C, Jen A K-Y, Schulten K and Baneyx F 2003 *Nat. Mater.* **2** 577
[83] Kjaergaard K, Sorensen J K, Schembri M A and Klemm P 2000 *Appl. Environ. Microbiol.* **66** 10
[84] Scembri M, Kjaergaard K and Klemm P 1999 *FEMS Microbiol. Lett.* **170** 363
[85] Manz A, Graber N and Widmer H M 1990 *Sensors Actuators* B **1** 244–8
[86] Ramsey J M and van den Berg A 2001 *Proc. μ TAS Symp.* (Dordrecht: Kluwer–Academic)
[87] Vellekoop M J, Lubking G W, Sarro P M and Venema A 1994 *Sensors Actuators* A **43** 175
[88] Mecea M V 1994 *Sensors Actuators* A **41/42** 630
[89] Snow A and Wohltjen H 1984 *Anal. Chem.* **56** 1411
[90] Suleiman A and Guilbault G G 1984 *Anal. Chim. Acta* **162** 97
[91] Ballantine D S, White R M, Martin S J, Ricco A J, Zellers E T, Frye G C and Wohltjen H 1997 *Acoustic Wave Sensors* ed R Stern and M Levy (San Diego, CA: Academic) p 36
[92] Slobodnik A J, Conway E D and Demonico R T 1973 *Microwave Acoustic Handbook, Surface Wave Velocities* (Bedford, MA: Air Force Cambridge Research Laboratories (LZM))
[93] Lundquist P M, Lin W P, Xu Z Y, Wong G K, Rippert E D, Helfrich J A and Ketterson J B 1994 *Appl. Phys. Lett.* **65** 1085
[94] Okano H, Tanaka N, Takahashi Y, Tanaka T, Shibata K and Nakano S 1994 *Appl. Phys. Lett.* **64** 166
[95] Brunner D, Angerer H, Bustarret E, Freudenberg F, Höpler R, Dimitrov R, Ambacher O and Stutzmann M 1997 *J. Appl. Phys.* **82** 5090
[96] Strite S and Morkoc H 1992 *J. Vac. Sci. Technol.* B **10** 1237
[97] Takikawa H, Kimura K, Miyano R, Sakakibara T, Bendavid A, Martin P J, Matzumuro A and Tsutsumi K 2001 *Thin Solid Films* **386** 276
[98] Caliendo C and Imperatori P 2003 *Appl. Phys. Lett.* **82** 1641